Coherent Optical Transceivers Scaling and Integration Challenges

This article addresses hardware and digital signal processing aspects of modern coherent optical transponders, which have revolutionized the optical communications industry over the past decade and have let commercial optical communication systems closely approach their fundamental limits.

By Takayuki Kobayashi , *Member IEEE*, Junho Cho , *Senior Member IEEE*, Marco Lamponi, Guilhem de Valicourt , *Senior Member IEEE*, and Christopher R. Doerr, *Fellow IEEE*

ABSTRACT | The advancement of digital coherent technologies has dramatically increased the system capacity per single-core single-mode fiber to the point that we can now approach the Shannon limit by utilizing high-order modulation formats and high-coding gain forward error correction (FEC) codes. Because the required energy per bit increases exponentially the closer we get to the Shannon limit, extending the available optical bandwidth by using ultrawideband wavelength-division multiplexing (WDM) and/or spatial-division multiplexing (SDM) is indispensable for increasing the system capacity with high energy efficiency. However, simple extensions of wavelength resources and spatial parallelization dramatically increase the number of transceivers (TxRxs) in proportion to the wavelength/spatial multiplicity. The key to achieving cost- and energy-efficient systems is to reduce the system complexity by using high-density integration and broadband optelectronics. In this article, we overview and discuss the recent advances of coherent optical transceivers integrated with an optical front end and digital signal processing (DSP)/application-specific integrated circuit (ASIC). We then present the transponder architectures and the challenges involved in applying them for massive parallelized transmission systems.

KEYWORDS | Digital coherent transceiver (TxRx); digital signal processing (DSP); fiber optics; integrated optics; silicon photonics.

NOMENCLATURE

ADC	Analog-to-digital converter.
AIR	Achievable information rate.
ASE	Amplified spontaneous emission.
ASIC	Application-specific integrated circuit.
AWG	Arrayed waveguide grating.
AWGN	Additive white Gaussian noise.
BPD	Balanced photodetector.
BPSK	Binary phase shift keying.
CC-MCF	Coupled-core multicore fiber.
CD	Chromatic dispersion.
CDM	Coherent driver modulator.
CMOS	Complementary metal–oxide–semiconductor.
CPO	Copackaged optics.
CW	Continuous wave.
DAC	Digital-to-analog converter.
DGD	Differential group delay.
DMD	Differential mode delay.
DSP	Digital signal processing.
EDFA	Er-doped fiber amplifier.
FEC	Forward error correction.
FMF	Few-mode fiber.
ICR	Intradyne/integrated coherent receiver.
IM-DD	Intensity modulation and direct detection.
IQM	IQ-modulator.
LO	Local oscillator.
MCF	Multicore fiber.
MC-FMF	Multicore few-mode fiber.

MZM	Mach–Zehnder modulator.
NLI	Nonlinear interference.
OSNR	Optical signal-to-noise ratio.
PBC	Polarization beam combiner.
PCB	Printed circuit board.
PCS	Probabilistic constellation shaping.
PDM	Polarization-division multiplexed/multiplexing.
PIC	Photonic integrated circuit.
PMD	Polarization mode dispersion.
QAM	Quadrature amplitude modulation.
QPSK	Quadrature phase shift keying.
RM	Rate matching.
RSOA	Reflective semiconductor optical amplifier.
SDM	Spatial-division multiplexing.
SERDES	Serializer and deserializer.
SGDBR	Sampled grating distributed Bragg reflector.
SMF	Single-mode fiber.
SNR	Signal-to-noise ratio.
SOA	Semiconductor optical amplifier.
TEC	Thermoelectric controller.
TIA	Transimpedance amplifier.
TL	Tunable laser.
WDM	Wavelength-division multiplexing.
WLL	Wavelength locker.
WSS	Wavelength selective switch.
ZF	Zero forcing.

I. INTRODUCTION

To meet the continuously increasing traffic demands driven by the expansion of bandwidth-hungry applications on high-speed mobile networks, the optical transport networks forming the backbone of wired and wireless communication services are constantly being improved due to recent advances in coherent transmission systems. In particular, WDM systems with an optical bandwidth exceeding 4 THz in the C-band (1530–1565 nm) or L-band (1565–1623 nm) used with digital coherent transceivers (TxRxs) have dramatically reduced transport costs in backbone networks [1]. In transmission systems using IM-DD before the digital coherent transmission era, the signal was typically transmitted by the intensity of the light wave (i.e., ON–OFF keying), which meant that the information rate was limited to 1 bit/symbol. Digital coherent technology [2] has made it possible to transmit a multitude of bits per symbol using the orthogonal signal dimensions of polarization, amplitude, and phase of light waves superimposed on the same time slot. Moreover, powerful DSP [2] has now enabled the compensation of signal distortion due to CD, PMD, and so on, which had greatly limited the transmission distance and the symbol rate in conventional IM-DD transmission systems. In digital coherent systems, these linear impairments no longer limit the transmission distance. Due to the advancement of digital coherent technologies, the capacity and channel rate per wavelength have both dramatically increased. Transoceanic-class transmissions with over-200-Gb/s channels and several-tens-Tb/s capacity have been reported in lab experiments [4], [5], [6], [7], [8], [9], [10]. One of the key enablers of such transmission rates is the high-speed transceiver offering digital linear/nonlinear compensation and advanced multilevel modulation formats combined with strong FEC codes. According to the Shannon theorem [11], the capacity of an AWGN channel increases (almost) logarithmically with the SNR and linearly with the bandwidth. In the AWGN channels, the SNR can arbitrarily be increased by increasing the signal power, but in optical fiber links, fiber nonlinear effects limit the maximum SNR and hence the capacity. Given the SNR limit imposed by the fiber nonlinear effects, the data rate has been increased by improving the spectral efficiency using a constellation size that best matches the SNR of the underlying channel. However, this is not power efficient due to the logarithmic increase of the data rate with signal power. In current WDM transmission systems, the capacity has also been increased by densely multiplexing Nyquist-pulse-shaped signals into wavelength channels within optically amplifiable bands. This increases the system capacity linearly with the number of multiplexed channels and, hence, with the total signal power increase. Therefore, the capacity increase by extending the available optical bandwidth has attracted much attention, especially for upgrading deployed-fiber links. By the simultaneous use of three bands, the C-band, L-band, and part of the S-band (1460–1530 nm)—ultrawide-bandwidth transmission experiments with an aggregate net data rate over 150 Tb/s have been reported [12], [13]. However, in SMF links, increasing the system capacity by extending the amplified bandwidth is typically limited due to a physical limit of the fiber input power known as a fiber fuse [14].

SDM [15] using parallel fibers or new fibers, such as multicore fibers and FMFs, is a promising technique to scale up the system capacity to over 1 Pb/s [16], [17], [18], [19], [20], [21]. In SDM systems, available wavelength resources are extended in proportion to the spatial multiplicities. However, there is a drawback in that the required number of transceivers is also increased to fill the spatial paths with signals. Therefore, broadband integrated transceivers, which can cover the wider optical bandwidth and high spatial multiplexities, are required for WDM/SDM transmission systems to reduce their system complexities.

In this article, we focus on transceiver structure scaling for future WDM/SDM transmission systems. In Section II, we present an overview of the current coherent transceivers and discuss the prospects for massive parallelization on the wavelength and spatial domains. Section III covers DSP techniques to increase the energy efficiency per bit and compensate for signal impairments. Section IV presents TL technologies for signals and LOs for parallelized transmission. In Section V, we describe PIC technologies based on silicon photonics offering both high integration density and low-cost packaging. We conclude
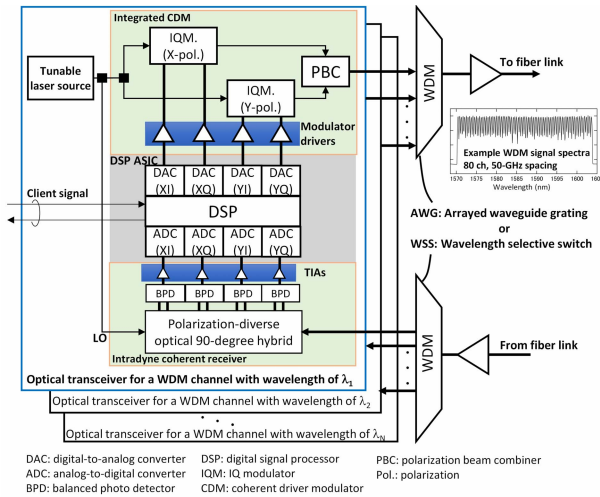
Fig. 1. *Schematic of coherent transceiver in a WDM transmission system.*

in Section VI with a brief summary and mention of future work.

II. COHERENT TRANSCEIVER STRUCTURE

In this section, we explain the structure of the coherent transceiver for single-core SMF. We then discuss the technical issues involved in scaling the current transceiver for massive parallelization.

A. Digital Coherent Transceiver

Fig. 1 shows an example of a transceiver configuration using digital coherent technology for single-core SMF transmission. A digital coherent transceiver consists of three elements: a transmitter, a receiver, and a DSP [22]. In the transmitter, the data bits of a client signal are interleaved and encoded to the code words of FEC codes. The encoded bits are then mapped to a symbol in the signal constellation (e.g., 64-ary QAM) at each polarization component. The encoded bits can potentially be formed through geometric [23], [24] or probabilistic [25] constellation shaping to mimic energy-efficient Gaussian signaling, before mapping to the constellation. Depending on the received signal processing method, a signal sequence known to both the transmitter and the receiver can be inserted for the synchronization of signal frames or pilot symbols can be inserted periodically to assist with adaptive signal processing such as carrier phase recovery and signal equalization. The data symbols are upsampled and subjected to waveform shaping with a Nyquist-pulse-shaped filter to limit the signal bandwidth. This makes it possible to transmit signals with an optical bandwidth similar to the symbol rate. Next, to improve the quality of the optical signal output from the optical modulator, the frequency responses of electrical and optical devices, such as DACs, modulator drivers, and optical IQMs, are corrected by a fixed equalizer [26]. This processing is performed in the digital domain on a DSP chip. The

digitized waveforms are converted to analog multilevel electrical signals by the DACs, and the CW light derived from a TL source is modulated by the optical IQM to generate an optical multilevel signal at a wavelength of λ_k. The polarization multiplexed signal is generated by coupling both polarization components via a PBC. A single WDM channel is generated in each optical transceiver, and multiple WDM channels are combined using an optical device such as an AWG or a WSS followed by an optical amplifier to recover the insertion loss. In this configuration, we can use the four orthogonal dimensions corresponding to amplitudes and phases in both polarization components for signal modulation.

At the receiver side, the received WDM signal is separated into each WDM channel using AWG or WSS. In each transceiver, the optical signal is converted into an electric signal by mixing it with CW light derived from a TL source (i.e., an LO) using a polarization diversity coherent receiver, namely, an ICR consisting of two optical 90° hybrids, four balanced receivers, and four TIAs. Then, the electrical analog received signal is sampled and quantized with ADCs. The receiver-side DSP for signal demodulation starts with correcting the imperfections of the optical and electrical devices in the receiver. Then, since the CD of the transmission fiber is static, it is compensated by a fixed equalizer [27]. Polarization demultiplexing is performed with an adaptive equalizer because the polarization state and polarization-mode dispersion dynamically change in fiber links. The receiver-side DSP adaptively compensates for the frequency and phase offsets between the transmitter laser and the LO. Finally, errors in the noisy recovered symbols are removed by an FEC decoder and an error-free transmitted bit stream is recovered. Fundamental DSP functions for coherent transceivers can be found in [2] and [3].

B. Challenges for Achieving Higher Speed Transceivers

Fig. 2 shows three ways to achieve commercial target net rates for a WDM channel. The first is to increase the
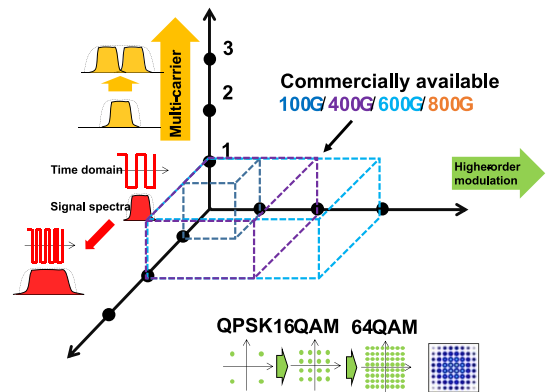

Fig. 2. *Three key elements of high-speed optical signals.*

symbol rate, namely, the modulation speed. In the case of fixing a modulation format, the line rate improves in proportion to the symbol rate and the required SNR does not change. Note that the required OSNR increases in proportion to the symbol rate because the noise bandwidth is fixed at 0.1 nm corresponding to about 12.5 GHz in the C-band by the OSNR definition [28]. Increasing the symbol rate is equivalent to expanding the occupied bandwidth of the signal spectra in the frequency domain. Therefore, high-symbol-rate transceivers require high-performance optical and electrical devices, such as DACs, modulator drivers, IQMs, BPDs, TIAs, ADCs, and DSP circuits. Increasing the symbol rate increases the net rate of a signal but does not improve the spectral efficiency, which is the rate of information per bandwidth. Therefore, the capacity of a WDM transmission system does not increase if an optical amplification bandwidth for WDM is not extended.

The second way is to utilize higher order modulation formats. By increasing the number of the amplitude and phase levels of light used for accommodating data bits encoded from a client signal, the information rate per bandwidth or "spectral efficiency" is improved. The maximum information rate for a given signal bandwidth is determined by $\log_2 (M)$ bits per polarization, where M is the number of symbol points in the signal constellation. However, as the modulation order increases, the requirements for the resolution and linearity of the devices (e.g., DACs, ADCs, and TIAs) increase. According to the Shannon limit, the required SNR increases exponentially when the number of bits to be transmitted per symbol increases. This means that the tolerance for signal distortion, and hence the transmission reach, decreases with increasing modulation order.

The third way is to use a multicarrier technology in which a channel is composed of multiple optical wavelengths (carriers). The net rate per channel can be improved in proportion to the number of carriers. However, when applying the multicarrier technology, the net rate, transmission performance, and cost per transceiver need to be considered because the number of required transmitters and receivers increases. Note that the "channel" here is the logical definition for network operation. In a physical layer, it is equivalent to WDM using few wavelengths.

High-speed optical transceivers have been put into practical use based on these three approaches. Widely deployed 100-Gb/s-class optical transceivers are implemented using polarization-division-multiplexed QPSK with a symbol rate of 32 GBd [29]. Early solutions for 400 Gb/s per channel were offered by the dual-carrier 32-GBd-class 16QAM signal [30]. Recently, the net rates per wavelength of commercially available transceivers have been increased up to 600 Gb/s using 64-GBd-class 64QAM signals [31], [32], [33] and 800 Gb/s using 100-GBd-class with 16QAM signals [34]. In [34], a 1.6-Tb/s transceiver with PICs and
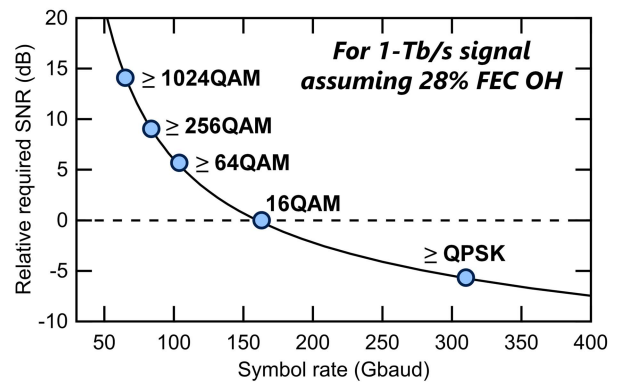

Fig. 3. *Relative required SNR for 1-Tb/s net rate as a function of symbol rate.*

one DSP ASIC chip for the dual-carrier signal, which can offer 2×800 Gb/s/λ, has been reported.

Digital coherent transceivers are configured by selecting the combination of discrete symbol rate and discrete constellation size depending on the target net rate and transmission distance. For increasing the constellation size of a 32-GBd signal from QPSK to 16QAM and 64QAM, discrete net rates of 100, 200, and 300 Gb/s can be achieved by assuming a fixed FEC overhead of ~20%. In order to achieve finer granularity of net rates, variable-rate FEC has been used [35]. In the current- and next-generation digital coherent transceivers, the optimal symbol rate for the device bandwidth and WDM spacing can be selected for nearly arbitrary net rates by almost continuously changing the constellation size using PCS [36]. The PCS also allows maximization of the net rates for any given SNR to approach the Shannon limit, offering a sensitivity gain compared with uniform QAM signaling. The definitions of line rates, information rates, and spectral efficiencies in optical transmission systems using PCS signals are described in [37].

Currently, research interest is moving toward high-speed transceivers beyond 1 Tb/s per wavelength. Fig. 3 shows the required SNR and symbol rate to achieve 1 Tb/s, where the required SNR is quantified relative to 16QAM assuming the FEC redundancy of 28%. For an information rate of 5 b/symbol (i.e., a net rate of 1 Tb/s with 64QAM at 106.7 GBd), an SNR at least 6 dB higher than 16QAM is required to maintain backward compatibility in terms of the transmission distance. The typical way to achieve a higher SNR is to reduce electrical noise and interference in the transceiver and optical ASE and fiber nonlinearities in the optical link. However, advanced DSP technologies, such as high-coding-gain FEC, PCS, and precise equalization as well as low-noise optical links consisting of low-loss and low-nonlinearity fibers with distributed Raman amplifiers [38], are already being actively deployed. Thus, further increasing the aggregate net rates in a single-core SMF

Table 1 Wavelength Bands

Band	Range (nm)
O-band	1260 to 1360
E-band	1360 to 1460
S-band	1460 to 1530
C-band	1530 to 1565
L-band	1565 to 1623
U-band	1623 to 1675

by improving SNR, DSP, FEC, and PCS is very difficult. It is therefore essential to develop an SDM technique that meets the continuous growth of capacity demands.

To obtain a high-quality, high-symbol-rate signal, it is important to minimize the narrowing of the signal band due to the frequency response of optical/electrical devices in the transceiver. Research and development of wideband devices is underway, and reports of high-speed modulators [39], [40] and broadband electrical amplifiers [41] have emerged. Two key devices in high-speed signal generation and detection are DACs and ADCs integrated with the DSP chip. High-speed ADCs with 110-GHz bandwidth and 256-GS/s sampling rate have been implemented in measurement equipment [42]. On the other hand, the analog bandwidth of the DAC using Si CMOS is expected to be about 50 GHz [43], which restricts the available symbol rate to 100 GBd according to the Nyquist theory. In recent years, several band expansion technologies have been proposed in which a plurality of CMOS DACs are bundled by a high-speed electric circuit and used as one wideband DAC [44], [45]. It is possible to generate high-symbol-rate signals beyond the limits of the CMOS DAC band limitation by integrating DSP and analog circuit technologies.

As we mentioned above, high-symbol-rate signals require a broad signal spectrum in the frequency domain so that wavelength resources for WDM in SMFs will be depleted because there are still technical challenges with wideband WDM in terms of extending the available optical bands from the conventional C- or L-bands to other bands such as O, E, and S (see Table 1) [46]. The most practical band extension involves using both the C-band and L-band, and optionally the S-band. Therefore, SDM is a promising approach to extend the available wavelength resources by using practical optical bands.

C. Classification of SDM

SDM is defined as a method of spatially multiplexing signals in some way. In the field of optical fiber communication, by introducing digital coherent technology, a 2-D spatial component in an SMF, namely, an orthogonal polarization component, is used to increase the spectral efficiency in the fiber without extra power penalty. To increase the spatial multiplexing density, it is important to newly develop transmission fibers with a structure that has multiple spatial paths in the cladding of an optical fiber. MCF, which has multiple single-mode cores in its cladding,

is highly compatible with conventional SMF transmission technology because the WDM signal can be transmitted independently for each core if the crosstalk between cores is sufficiently suppressed or managed [47]. A coupled-core (CC) MCF has been proposed in which the distance between the cores of an MCF is shortened to intentionally generate crosstalk between them [48]. MIMO signal processing is required at either or both the transmitter and the receiver to separate signals mixed in CC-MCF links. FMF uses multiple fiber propagation modes [49]. Similar to CC-MCF transmission systems, FMF transmission systems require MIMO signal processing in the receiver because the signals input to modes at a wavelength are coupled with each other in the fiber propagation. Furthermore, to increase the spatial multiplicity, an MC-FMF in which each core has multiple propagation modes has also been proposed [50], [51]. Due to its complicated structure, sophisticated technologies are required for manufacturing and connection, but it is a promising transmission medium for achieving spatial multiplicities of 100 or more.

D. Challenges for SDM Transceiver

Fig. 4 shows the schematic of an optical transceiver for the WDM/SDM transmission system. The basic idea is to integrate the coherent transceivers shown in Fig. 1 by spatially multiplying M. CW light with a wavelength of λ_k derived from a TL source is shared by totally $2M$ pieces of CDMs and ICRs. Because low input powers to CDMs and ICRs cause fatal SNR degradation, this requires the higher output power of a TL source by at least M-fold while maintaining a narrow linewidth to achieve the same power budget of a conventional transceiver. Another option is to place optical amplifiers at the input of CDMs and ICRs, although this would increase the number of components. For uncoupled SDM transmission systems, parallel CDMs can be
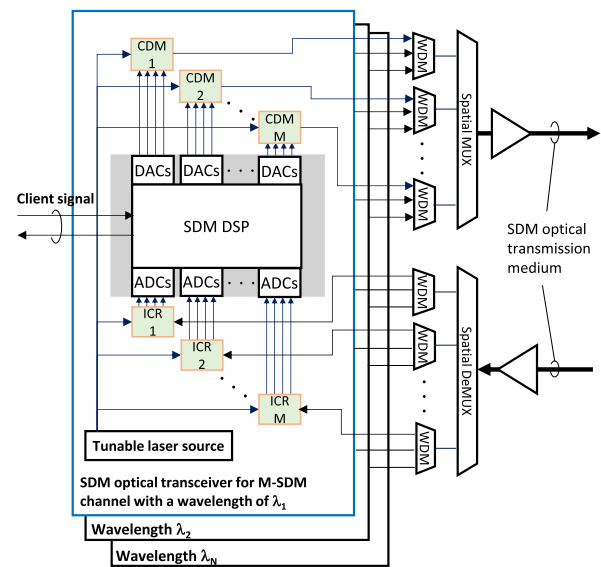

Fig. 4. *Schematic of SDM optical transceiver with M spatial multiplicity in an N-ch. WDM transmission system.*

driven by independent DACs and transmitter-side DSPs because MIMO processing is unnecessary between spatial modes. The same applies to ICRs, ADCs, and receiver-side DSPs. On the other hand, coupled SDM transmission systems require MIMO processing, and CDMs with DACs and DSP at the transmitter-side need to operate in synchronization. At the receiver side, digitized received signals from all ADCs, which must be synchronized with each other, are required for signal demodulation with MIMO processing. Thus, these DACs, ADCs, and DSPs should be implemented in one ASIC chip. However, compared to the conventional coherent DSP for the SMF transmission, the circuit size is at least M times larger. Moreover, regarding SDM MIMO processing, its computational complexity is increased in proportion to the square of M compared to that of polarization demultiplexing using 2×2 MIMO processing in SMF transmission systems. In the case of an SDM MIMO implementation with multiple DSP chips, $M \times 1$ MIMO processing is implemented in each DSP chip; however, ultrahigh-speed interconnections are required because digitized waveform data are transferred from all ADCs to each DSP chip. In both coupled and uncoupled SDM, high-density integration with low power consumption is essential to achieve cost-effective SDM optical transceivers. In Fig. 4, spatial (de-) multiplexers are placed outside the integrated transceiver because their structures strongly depend on the SDM transmission media. For example, in FMF transmission systems, if multimode AWG can be developed, it might be possible to integrate spatial (de-) multiplexing devices into each transceiver.

III. DIGITAL SIGNAL PROCESSING

In this section, we first describe a simplified channel model for PDM SDM systems, without considering diverse physical factors such as DGD spread across modes, Kerr effect, and transceiver impairments. Using this simplified SDM channel model, we evaluate the capacity of PDM SDM systems. We then consider the real-world factors mentioned above and discuss the entire DSP chain for true SDM systems and the challenges in integrating it on an ASIC chip. In the mathematical expressions that follow, we use a nonboldface letter for a scalar (e.g., x or X), a boldface lowercase letter for a vector (e.g., $\mathbf{x}$), and a boldface capital letter for a matrix (e.g., $\mathbf{X}$), unless otherwise specified.

A. Channel Model and Capacity of Idealized SDM Systems

Disregarding the DGD spread, Kerr effect, and transceiver impairments, a PDM SDM system can be expressed as an MIMO channel

$$\mathbf{y} = \mathbf{Hx} + \mathbf{n} \tag{1}$$

where $\mathbf{x} \in \mathbb{C}^{2M \times 1}$ and $\mathbf{y} \in \mathbb{C}^{2M \times 1}$ are transmitted and received complex-valued signal vectors over M spatial

modes with two polarization modes each, respectively, $\mathbf{H} \in \mathbb{C}^{2M \times 2M}$ is a channel matrix that represents random mode coupling, and $\mathbf{n} \in \mathbb{C}^{2M \times 1}$ is an ASE noise vector that consists of $2M$ independent circularly symmetric Gaussian noises of the same variance σ_n^2, i.e., $\mathbf{n} \sim \mathcal{CN}(0, \sigma_n^2 \mathbf{I})$ with $\mathbf{I}$ being an identity matrix. By singular value decomposition, the channel matrix can be factorized into three $2M \times 2M$ square matrices as

$$\mathbf{H} = \mathbf{U \Lambda V}^H \tag{2}$$

where $(\cdot)^H$ denotes the conjugate transpose, $\mathbf{U}$ and $\mathbf{V}$ are unitary matrices, and $\mathbf{\Lambda}$ is a diagonal singular value matrix expressed as

$$\mathbf{\Lambda} = \begin{bmatrix} \lambda_1 & 0 & \cdots & 0 \\ 0 & \lambda_2 & \cdots & 0 \\ \vdots & \vdots & \ddots & \vdots \\ 0 & 0 & \cdots & \lambda_{2M} \end{bmatrix}. \tag{3}$$

Here, λ_m quantifies the gain or loss of the mth mode that remains when the mode mixing by the unitary matrices $\mathbf{U}$ and $\mathbf{V}$ is perfectly reverted. In an ideal SDM system, all λ_m are 1, and hence, (2) degenerates to a single unitary matrix $\mathbf{H}$, but in practice, the spread of λ_m appears due to the mode-dependent gain of optical amplifiers or the MDL of inline elements such as fibers, splices, connectors, mode multiplexers, AWGs, or WSSs, which reduces the capacity (as described in the following).

To evaluate the theoretical limit of communication in SDM systems, we assume perfect knowledge of $\mathbf{H}$ at both the transmitter and the receiver. The transmitter performs precoding as $\hat{\mathbf{x}} = \mathbf{Vx}$ such that the channel becomes

$$\mathbf{y} = \mathbf{U \Lambda V}^H \hat{\mathbf{x}} + \mathbf{n} = \mathbf{U \Lambda x} + \mathbf{n} \tag{4}$$

and the receiver uses a ZF equalizer given by

$$\mathbf{W} = \mathbf{\Lambda}^{-1} \mathbf{U}^H \tag{5}$$

such that the transmitted signal can be recovered as

$$\tilde{\mathbf{x}} = \mathbf{Wy}. \tag{6}$$

Then, the concatenation of the SDM channel (4) and ZF equalization (6) leads to

$$\tilde{\mathbf{x}} = \left(\mathbf{\Lambda}^{-1} \mathbf{U}^H \right) (\mathbf{U \Lambda x} + \mathbf{n}) = \mathbf{x} + \mathbf{n}' \tag{7}$$

where $\mathbf{n}' = \mathbf{\Lambda}^{-1} \mathbf{U}^H \mathbf{n}$ is a noise vector whose elements are independent of each other and the mth element is circularly symmetric Gaussian with variance σ_n^2 / λ_m^2, i.e.,
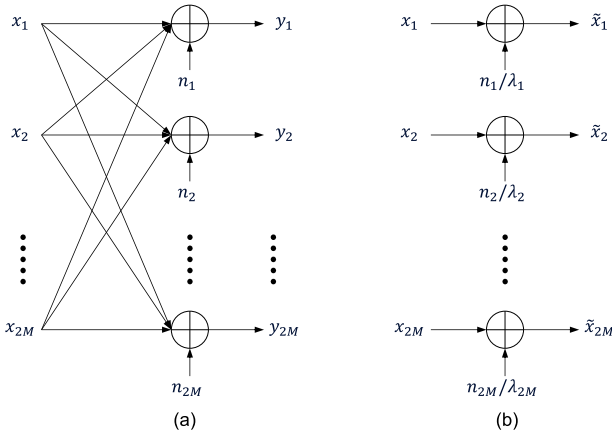
Fig. 5. *(a) Strongly coupled SDM channel model and (b) equivalent SDM channel model obtained by precoding and ideal ZF equalization.*

$\mathbf{n'} \sim \mathcal{CN}(0, \sigma_n^2 \mathbf{\Lambda}^{-2})$. Therefore, the ZF equalization transforms the SDM channel (1) into parallel (uncoupled) unit-gain Gaussian channels (7), as shown in Fig. 5. If a transmit power constraint is imposed on the total power over all modes, water-filling power allocation [52] can be performed as

$$P_m = \left[\mu - \sigma_n^2 / \lambda_m^2 \right]^+ \tag{8}$$

where P_m is the power of x_m, $[x]^+$ denotes $\max(x, 0)$, and the water level μ is determined such that the total power constraint $\sum_{m=1}^{2M} P_m = P_{\text{Tot}}$ is fulfilled. The SNR of the mth mode is then calculated as

$$\text{SNR}_m = \lambda_m^2 P_m / \sigma_n^2. \tag{9}$$

On the other hand, if a transmit power constraint is imposed on individual modes, the transmitter allocates an equal transmit power $P_{\text{Tot}}/(2M)$ to all x_m for $m = 1, \ldots, 2M$. In this case, the SNR of the mth mode is calculated as

$$\text{SNR}_m = \lambda_m^2 \bar{\text{SNR}} \tag{10}$$

where we define the total SNR as $\bar{\text{SNR}} = P_{\text{Tot}}/(2M\sigma_n^2)$. Note that the ZF equalizer in (5) is merely a rotation of the measurement axis followed by scaling to make the channel have unit gain, and the MMSE equalizer produces the same SNR as the ZF equalizer in this system. Regardless of whether the transmit power constraint is applied across all modes or for individual modes, the average channel capacity per mode of this system can be obtained as

$$C = \frac{1}{2M} \sum_{1}^{2M} \log_2 \left(1 + \text{SNR}_m\right). \tag{11}$$

This shows that, for fixed launch P_{Tot} and ASE power $2M\sigma_n^2$ (hence for a fixed SN̄R), the capacity can change depending on random realizations of λ_m, as quantified in the following. Indeed, (11) represents the capacity limit rather than capacity, for reasons explained later. Note that λ_m for $m = 1, \ldots, 2M$ are not independent of each other, but they should satisfy the condition

$$\sum_{m=1}^{2M} \lambda_m^2 P_m = P_{\text{Tot}} \tag{12}$$

assuming that SDM systems are configured to have unit gain in terms of total power over all modes.

The MDL is defined as

$$\text{MDL} = \frac{\max\left(\lambda_m^2\right)}{\min\left(\lambda_m^2\right)}. \tag{13}$$

The MDL increases approximately in proportion to the square root of the transmission distance [53], [54]. For MDL = 0, 5, 10, 15, and 20 dB, Fig. 6 shows the average capacity per mode of an SDM system with $2M = 6$ as a function of SN̄R, with (solid lines) and without (dashed lines) water filling. Here, we assume that λ_m^2 are uniformly distributed when expressed in decibels.[1] We can observe in the figure that the capacity limit is maximized by MDL = 0 dB (blue lines) and decreases with increasing MDL. The

[1]Note that even for the same MDL, the set of λ_m can vary depending on SN̄R. Assuming water-filling power allocation with MDL > 0 dB and hence $P_i \neq P_j$ for $i \neq j$, the unit-gain condition (12) is fulfilled by different λ_m values at different SN̄R values for the same MDL. For example, given $2M = 6$ and MDL = 10 dB, the condition (12) is satisfied by $\lambda_m^2 \approx \{-7.5, -5.5, \ldots, 2.5\}$ at SN̄R of 5 dB, but it is satisfied by $\lambda_m^2 \approx \{-6.3, -4.3, \ldots, 3.7\}$ dB at SN̄R of 20 dB, where in both cases, λ_m^2 is uniformly distributed in decibel and MDL = $\max(\lambda_m^2)/\min(\lambda_m^2) = 10$ dB.
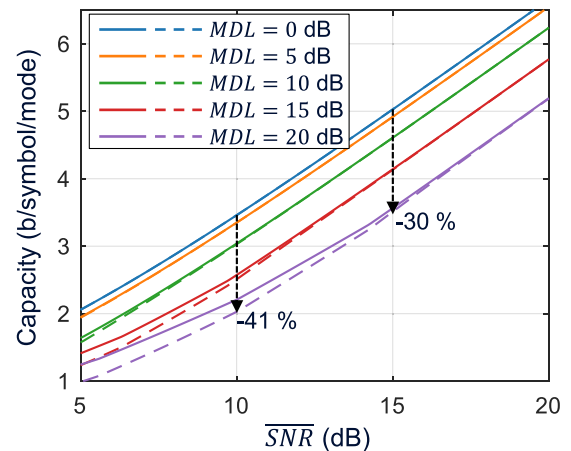

Fig. 6. *Mode-averaged capacity limits of an SDM system with $2M = 6$ modes, with (solid lines) and without (dashed lines) water filling. Singular values of H are uniformly distributed for MDL = 0, 5, 10, 15, and 20 dB.*
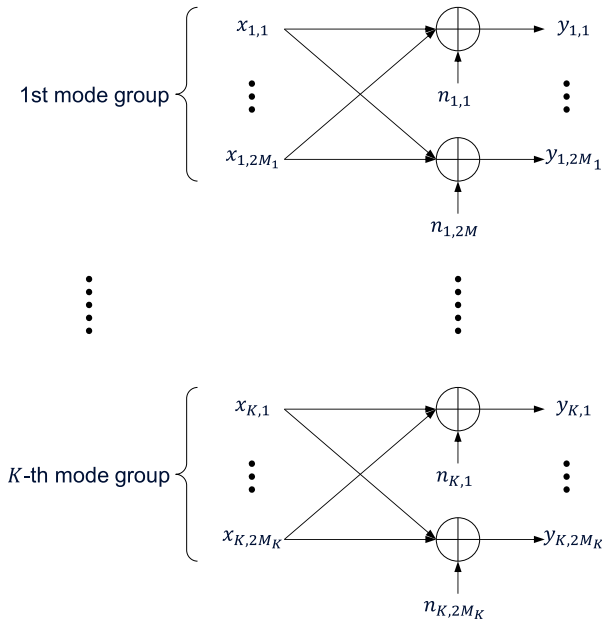
Fig. 7. *Weakly coupled SDM channel model.*

decrease in capacity limit due to MDL can be substantial, as the MDL can reach $\sim$16 dB at 3500 km [55].

In the SDM systems described above, all modes are randomly mixed (in this case, the modes are called strongly coupled). However, if the mode mixing occurs only within each mode group but not between mode groups (in this case, the modes are referred to as weakly coupled), the fully connected channel model in Fig. 5(a) can be split into smaller independent sets of parallel SDM channels, as shown in Fig. 7. In this case, the unitary matrices $\mathbf{U}$ and $\mathbf{V}$ can be represented as blockwise unitary matrices

$$\mathbf{U} = \begin{bmatrix} \mathbf{U}_1 & \mathbf{0} & \cdots & \mathbf{0} \\ \mathbf{0} & \mathbf{U}_2 & \cdots & \mathbf{0} \\ \vdots & \vdots & \ddots & \vdots \\ \mathbf{0} & \mathbf{0} & \cdots & \mathbf{U}_K \end{bmatrix} \quad (14)$$

and

$$\mathbf{V} = \begin{bmatrix} \mathbf{V}_1 & \mathbf{0} & \cdots & \mathbf{0} \\ \mathbf{0} & \mathbf{V}_2 & \cdots & \mathbf{0} \\ \vdots & \vdots & \ddots & \vdots \\ \mathbf{0} & \mathbf{0} & \cdots & \mathbf{V}_K \end{bmatrix} \quad (15)$$

where K is the number of mode groups, $\mathbf{U}_k$ and $\mathbf{V}_k$ for $k = 1, \ldots, K$ are small unitary matrices representing the kth mode group, and $\mathbf{0}$s are zero matrices. The SDM equation (1) with a large-dimensional matrix and vectors can also be split into K equations with small-dimensional matrices and vectors as

$$\mathbf{y}_k = \mathbf{H}_k \mathbf{x}_k + \mathbf{n}_k \quad (16)$$

where $\mathbf{H}_k = \mathbf{U}_k \mathbf{\Lambda}_k \mathbf{V}_k^H$ is the channel matrix of the kth mode group with singular value matrix $\mathbf{\Lambda}_k$. Since (16) describes a smaller SDM subsystem of the large SDM system (1), the precoding and ZF equalization can be performed on (16) similar to those on (1), and the capacity limits can be obtained correspondingly.

The capacity limit (11) is an upper bound of the capacity of SDM systems for various reasons. First, it assumes that the channel $\mathbf{H}$ is perfectly known to both the transmitter and receiver, whereas the transmitters in practical optical systems do not know $\mathbf{H}$ and the receivers have only an estimate of $\mathbf{H}$ with estimation errors. Second, it assumes that the channel is stationary and the singular values λ_m [and hence SNR_m, cf. (10)] do not vary in time. Theoretically, if the channel statistics are known by long-term average, the ergodic capacity is obtained by averaging (11) over an ensemble of channel states. However, if the channel state varies just slowly in time, a more practically relevant metric is the outage capacity, which we will discuss briefly in Section III-B. Third, (11) considers the ASE noise only, neglecting the NLI due to the optical Kerr effect. In many optical systems, the NLI is treated as Gaussian noise because of the intricacies involved in canceling the NLI by DSP. As the NLI is treated as additive noise, its presence in optical channels only decreases the capacity compared to (11). A potentially significant advantage of SDM systems over single-mode systems is that the NLI decreases as the number of strongly mixed modes increases [56], [57], for a similar reason that it decreases as CD increases [58]. Namely, just as the CD causes multiple signals to be mixed in time, SDM causes multiple signals to be mixed in space. Therefore, the reduction of capacity due to NLI tends to be smaller in strongly coupled SDM systems than in single-mode or weakly coupled SDM systems, provided that MDL is not significant. However, approaching the capacity of strongly coupled SDM systems entails several practical challenges, as will be discussed in Section III.

The capacity limit (11) and the underlying SDM channel model in Fig. 5(b) tell us which PCS and FEC implementation architecture allows us to achieve capacity. We first note that the capacity of each decoupled mode in Fig. 5(b) is achieved by continuous Gaussian signaling as per Shannon's findings [11], and its variance is given by the water-filling principle (8). This suggests that when approximating Gaussian signals using discrete modulation, the PCS rate should be independently optimized for each mode. Even with uniform power allocation, the PCS rate should be independently optimized for each mode to approach capacity due to the mode-dependent SNR as given in (10), and the FEC rate should also be optimized for each mode accordingly. The procedure to find the right PCS and FEC rates for a given SNR is commonly referred to as RM, and it can be done, for example, in the manner described in [36] and [59].

Although mode-individual RM maximizes the theoretical AIR of the system, there may be cases where it is
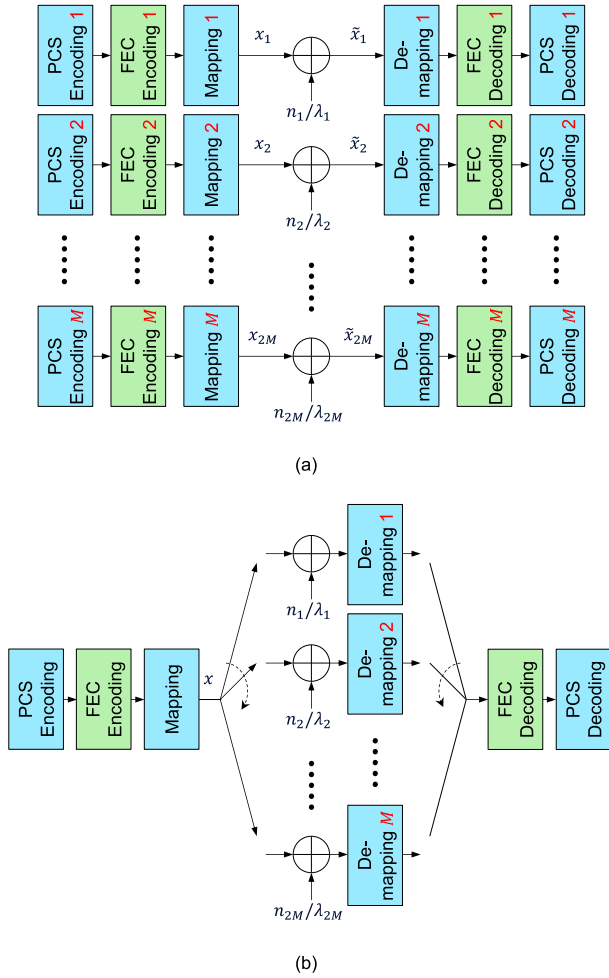
(a)

(b)

Fig. 8. *Systems with PCS and FEC matched (a) individually for each mode and (b) once for all modes.*
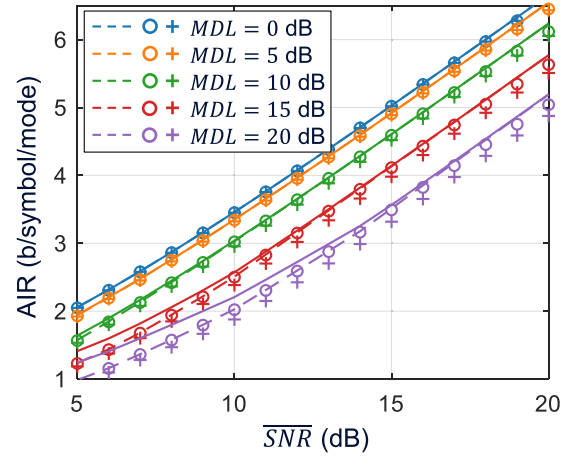

Fig. 9. *Mode-averaged AIR of an SDM system with $2M = 6$ modes using binary FEC and PCS 256-QAM without water-filling. PCS and FEC rates are matched individually for each mode (circle markers) or once for all modes (plus markers). The dashed lines in Fig. 6 are reproduced here for reference. Singular values of H are uniformly distributed for MDL $= 0$, 5, 10, 15, and 20 dB.*

This penalty arises from the use of suboptimal RM due to the constraints of the system architecture shown in Fig. 8(b). Since the channel capacity is the greatest of all AIRs for a given channel, it is not surprising that the gap between AIR and capacity grows as more and more constraints (discrete modulation, binary code, and system architecture) are imposed.

B. DSP for SDM Systems

To compensate for real-world impairments such as DGD spread and transceiver impairments, DSP is required in SDM systems. DGD between spatial modes is also referred to as DMD in SDM systems. At the transmitter, the DSP for an SDM system with $2M$ modes is merely M copies of the DSP for a single-mode system, except when PCS or FEC is performed jointly over multiple modes. More differences in DSP can be found at the receiver between SDM and single-mode systems, as shown in Fig. 10.
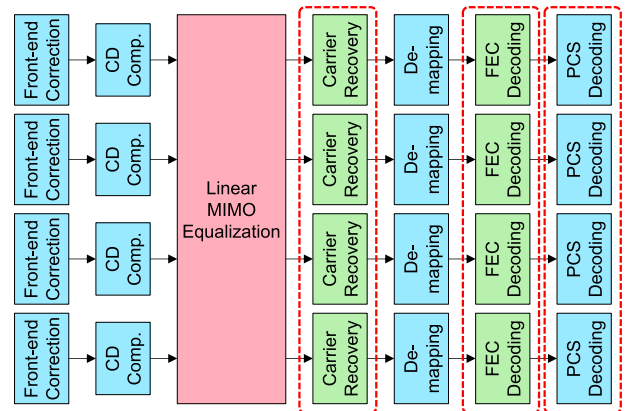

Fig. 10. *Receiver-side DSP for strongly coupled SDM systems.*

preferred to use a single FEC code and a single PCS code for the entire system, as shown in Fig. 8(b), for example, for implementation reasons. In this case, RM is performed only once for the entire system, which we refer to as the mode-group RM scheme. Since the PCS and FEC rates matched for all modes in an average sense are mismatched for individual modes, the mode-group RM reduces the AIR compared to the mode-individual RM. For the same MDL $= 0$, 5, 10, 15, and 20 dB as in Fig. 6, the AIR per mode of an SDM system with $2M = 6$ is shown in Fig. 9, using binary FEC and PCS 256-QAM without water filling. Looking at the mode-individual RM, the decrease of AIR by PCS 256-QAM (circle markers) relative to capacity (dashed lines) increases with increasing $\overline{SNR}$ and increasing MDL. This performance penalty is attributed to the constraints of using discrete modulation and binary FEC compared to the case of unconstrained Gaussian signaling. Looking at PCS 256-QAM, the decrease of AIR by mode-group RM (plus markers) relative to mode-individual RM (circle markers) also increases with increasing $\overline{SNR}$ and increasing MDL.

The biggest difference of the receiver-side DSP is that, as mentioned in Section III-A, channel equalization is performed across $2M$ modes in SDM systems, as opposed to just two polarization modes in single-mode systems. Here, we assume a strongly coupled SDM system, without loss of generality since weakly coupled SDM systems are a set of strongly coupled SDM systems. Linear adaptive MIMO equalizers are commonly used for channel equalization in the form of a $2M \times 2M$ complex-valued equalizer as

$$\text{(Filtering)} \quad \tilde{\mathbf{x}} = \mathbf{W}\mathbf{y} \tag{17}$$

and

$$\text{(Adaptation)} \quad \mathbf{W} = \mathbf{W} + \mu \mathbf{e}\mathbf{y}^H \tag{18}$$

where μ is the step-size parameter. For the least mean square (LMS) algorithm, the error vector $\mathbf{e}$ can be obtained as

$$\mathbf{e} = D\left(\tilde{\mathbf{x}}\right) - \tilde{\mathbf{x}} \tag{19}$$

where $D(\cdot)$ denotes the elementwise hard decision of symbols. For the constant modulus algorithm (CMA), the error vector can be obtained as

$$\mathbf{e} = \tilde{\mathbf{x}} \odot \left(r - |\tilde{\mathbf{x}}|^{\circ 2}\right) \tag{20}$$

where $r = E(|x|^4)/E(|x|^2)$ with $E(\cdot)$ being the expectation operator and $\odot$ and $|\cdot|^{\circ 2}$ denoting elementwise multiplication and elementwise absolute square, respectively. The computation of (17) requires $O(M^2)$ complex multiplications, and the computation of (18)–(20) requires $O(M)$ complex multiplications. Therefore, (17) determines the complexity of the MIMO equalizer, which increases quadratically with the number of coupled modes.

For convenience of explanation, we assume above that there is no intersymbol interference within each mode and no DGD spread across modes. In real SDM systems, however, the DGD spread across modes generally increases with transmission distance and with the number of coupled modes due to mode mixing and group velocity dispersion. Therefore, the linear adaptive equalizer $\mathbf{W}$ in (17) must be a 3-D matrix of size $2M \times 2M \times L$, with $2M \times 2M$ being the number of taps in each time slot and L being the number of time slots (i.e., the filter memory length) to compensate for the DGD spread. The equalizer length L has a significant impact on the DSP complexity of an SDM system, so we discuss in detail next how L varies with system parameters.

Let t_m be the DGD of the mth mode relative to the average propagation time of all modes, i.e., the DGDs have zero mean such that $\sum_{m=1}^{2M} t_m = 0$. Without loss of generality, assume that the DGDs are sorted in an ascending order as $t_1 < \cdots < t_{2M}$. Then, the equalizer must include all signals

from time t_1 to time t_{2M}, so its length L is proportional to the maximum DGD difference $\Delta t = t_{2M} - t_1$ (except when no mode mixing occurs and no MIMO equalizer is needed). The DGD spread is often defined as twice the standard deviation of t_m as $\sigma_\tau = 2(1/(2M) \cdot \sum_{m=1}^{2M} t_m^2)^{1/2}$ [60], [61], [62]. If t_m for $m = 1, \ldots, 2M$ is uniformly distributed at regular intervals, the maximum DGD difference in the absence of mode mixing can be obtained from the DGD spread as $\Delta t = \sigma_\tau(3(2M - 1)/(2M + 1))^{1/2}$. In the case that $M = 1$ (i.e., in SMF), this degenerates to $\Delta t = \sigma_\tau$, and as M goes to infinity, $\Delta t \rightarrow \sqrt{3}\sigma_\tau$. When there is no mode mixing, t_m is a deterministic variable that increases linearly with propagation distance, so Δt and σ_τ also increase linearly with distance. On the other hand, when there is strong mode mixing, t_m can be treated as a random variable that follows a Gaussian-like distribution when M is small and tends toward the ideal Gaussian as M grows [60], [61], [62], [63]. Since t_m has zero mean, its Gaussianity implies that σ_τ alone can completely define the distribution of t_m, and furthermore, σ_τ grows only with the square root of the distance [60], [61], [62]. This represents the advantage of strong mode mixing in reducing the MIMO equalizer length L in long-haul SDM systems. Since Δt also increases linearly with the number of modes, the overall MIMO equalization complexity increases as $O(M^3 z^{1/2})$ in strongly coupled SDM systems, with z being the propagation distance, whereas it increases only as $O(M)$ independently of the distance in uncoupled SDM systems. To date, a DGD spread of $\sigma_\tau = 3.14 \pm 0.17$ ps/km$^{1/2}$ has been reported using a four-core CC-MCF [62]. With this DGD spread, intersymbol interference over a time interval of $\alpha \cdot \sigma_\tau$ for $\alpha = 1, 2, \ldots$ can be compensated, e.g., by using $L = 63\alpha$ half-symbol-spaced equalizer taps in a 100-GBd SDM system. When intersymbol interference spans many time slots, the equalization complexity can be reduced to $O(M^2 \log M z^{1/2})$ by using frequency-domain equalizers with fast Fourier transform (FFT) (see [64] and [65]). The higher-than-quadratic complexity of MIMO equalization with respect to the number of coupled modes is perhaps one of the biggest challenges in DSP, as it hinders the deployment of strongly coupled SDM systems and makes weakly coupled SDM systems a more viable option. In SDM systems, both DGD and MDL are highly dependent on the link configuration such as the type of SDM fibers and optical amplifiers and have frequency dependence [66]. Since their combined effect can cause degradation of SNR at a specific frequency of the signal even if DGD is compensated by a linear equalizer, DSP must consider the outage probability of the system [67].

In the case where the LMS algorithm is used for MIMO equalization, the carrier recovery in Fig. 10 should be integrated into the equalizer because the LMS algorithm requires a hard decision of symbols (and hence the carrier recovery), as shown in (19). On the other hand, if the CMA is used for MIMO equalization, the carrier recovery can be performed after the MIMO equalization. In cases where high correlations are observed between the carrier phase

errors of coupled modes [68], the carrier recovery can be performed jointly over coupled modes, as indicated by the first red dashed box in Fig. 10.

Another receiver-side DSP that can be jointly performed over modes is the FEC decoding and PCS decoding, as indicated by the next two red dashed boxes in Fig. 10 (this requires joint PCS encoding and joint FEC encoding over modes in the transmitter as well). As discussed in Section III-A, the SDM channel capacity (11) can be approached only if FEC and PCS are performed with mode-individual RM [cf. Fig. 8(a)]. If the singular values λ_m (and hence SNR_m) are time-invariant, the perfect matching of the FEC and PCS rates to the underlying channel states is possible by acquiring SNR_m just once when the fiber is first deployed. However, in practice, λ_m and SNR_m vary in time, and in general, no feedback channel is available when the network is in service. Therefore, it is not possible to match the FEC and PCS rates to the underlying channel states at all times, and (11) only represents an upper bound of capacity. A pragmatic approach to maximizing the net data rate is to use a single FEC code and a single PCS code with mode-group RM [cf. Fig. 8(b)], with some margin to account for a stochastic singular value spread. If the singular value spread is stationary and the symbols are interleaved in time and modes using an infinite-length interleaver, a single FEC code of infinite length can maximize the net data rate by maximizing the FEC code rate while achieving a vanishingly small outage probability. However, when using a finite-length interleaver and a single finite-length FEC code, a lower code rate compared to the infinite-length counterpart should be used under a pessimistic assumption. If the singular values λ_m change slowly over time, the channel coherence time can exceed the finite FEC code word duration, and the code words transmitted during poor channel states can cause outage. To avoid this outage, a lower code rate than assuming constant channel conditions or infinite code length must be used, which reduces net data rates.

If the FEC or PCS coding is implemented as joint processing over multiple modes, the degree of parallelism should increase in proportion to the number of modes to meet the net throughput requirements that increase at the same rate as the number of modes, that is, in the case of mode-individual FEC and PCS, $2M$ devices independently process the payload for each mode, so a degree of parallelism of $2M$ is inherent. On the other hand, in the case of mode-group FEC and PCS, one device combines and processes the payloads for all modes, so a degree of parallelism of $2M$ must be achieved inside the device. This requires the construction of FEC or PCS codes capable of massively parallel processing within a single code word, which can potentially pose challenges in ASIC implementations. Therefore, if the singular values of the SDM channel matrix are slowly time-varying, FEC may favor weakly coupled SDM systems over strongly coupled SDM systems due to the potential difficulty in achieving the required parallelism.

IV. LASERS

As shown in Fig. 1, TLs are a key component of coherent TxRxs for the operation of WDM systems. One coherent TxRxs include a transmitter laser and a receiver laser that can be separated or a single laser. In the latest transceiver, the output light of such a TL is split between the transmitter and the receiver acting as a photon supply for the transmitter and LO for the receiver. At this point, TLs integrated with a PIC have been commercially deployed for III–V-based transceivers but not for silicon-based PIC, leading to the use of an external TL source.

A TL requires a TEC in order to precisely tune the output power and the emitted wavelength independently of external temperature variation. The power consumption of the TEC is roughly proportional to the chip size and represents a significant fraction of the overall power consumption. For this reason, whenever a TEC is not required on the TxRx side, the cointegration of the laser with the TxRx is not convenient from a cost perspective and the LO is packaged separately.

For a massively parallel WDM/SDM long-haul coherent system, we expect multiple TLs to be integrated separately from the TxRx. However, as coherent technologies are expected to conquer a large market share in metropolitan and inter datacenter networks in the very near future, laser integration with coherent PIC has also been investigated [69].

Hybrid integrated TLs are based on a compact gain medium where a semitransparent mirror is placed at the output side to enable the light emission and a high-reflectivity mirror closes the cavity. This configuration creates multiple reflections inside the cavity that induce lasing on multiple longitudinal modes. Mode selection is achievable by introducing an intracavity filter. For example, an external cavity TL consisting of a gain chip and separate bulky optical filters has been widely used in coherent lightwave transmission experiments. In this section, we review the requirements and recent advances of integrated III–V and hybrid III–V/SOI/SiN TL.

A. Laser Requirements for Coherent Transmission Link

Laser phase noise induces phase rotation for the constellation points along a constant radius which can create interference in a dense constellation format, as shown in Fig. 11. Therefore, narrow linewidth lasers become critical, especially for the 64QAM modulation format. Furthermore, in a high symbol rate and/or long-distance system, equalizer-enhanced phase noise imposes even stronger requirements on the TL linewidth.

High output power (usually up to 16 dBm) is needed, especially at the transmitter side, where high modulation loss occurs due to the high modulation format (e.g., the modulation loss due to 64QAM is 3–3.5 dB higher than that of QPSK) and the insertion loss of the transmitter itself
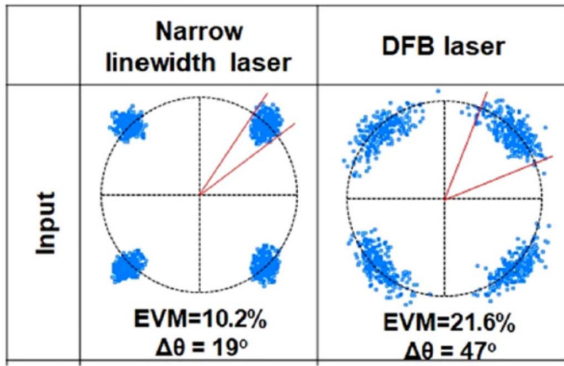
Fig. 11. *Impact of laser linewidth on constellation points for QPSK modulation format [70].*

needs to be compensated, especially for silicon-photonic transmitters. The output of the TL can be shared between the Tx and the Rx and even between multiple TxRxs for an SDM system (as detailed in Section II-D), thus increasing the need for high output power TL.

A wide tuning range is also required for WDM systems over the C-band, and also the C- and L-bands for ultrahigh-capacity systems. Recently developed TLs cover 6 THz ($\sim$50 nm) in order to keep the same number of channels (80) as legacy systems but with a 75-GHz spacing to accommodate a 64-GBd signal.

Finally, lower power consumption and a compact footprint are vital for pluggable coherent transceivers (as opposed to line-card-based systems). New form factors such as QSFP-DD have even stricter requirements on space and power consumption when integrating TL.

B. Gain Medium

For applications centered on data communication networks (built around the 1310-nm wavelength) and telecommunication networks (built around the 1550-nm wavelength), III–V materials can provide optical gain via electrical injection in a wide wavelength range using both interband and intraband transitions. SOAs are often used as a compact gain medium for external cavity TLs. Light emission and/or amplification is provided using III–V material gain, and hybrid solutions that combine III–V and silicon/SiN/SiO$_2$ materials are being investigated for integrated TLs. However, the optical gain bandwidth of the III–V material is usually limited to 30–40 nm. Since long-distance dense-WDM systems are running out of channels in the C- and L-bands, the Raman amplification technology should prove useful [71]. WDM systems will require upgrading in order to meet the rise in bandwidth demand by exploring another spectral region (as detailed in Section II-B). Ultrawide bandRSOA has been investigated, where large optical gain controlled by current injection can be obtained. In [72], the RSOA consists of a 3-mm-long waveguide with an MQW InGaAsP lightly coupled active zone ($\Gamma \sim 4\%$). The broadening of the ASE

bandwidth can reach up to 111 nm at 380 mA, as shown in Fig. 12. Such wide optical gain is vital to obtain a wide tuning range and 95 nm over the C- and L-bands, which has been demonstrated.

C. CoIntegration Approaches

Several platforms and approaches have been proposed for the integration of TLs over the last ten years. For simplicity, we divide these into active material platform, passive resonator platform, and hybrid integration approach.

The active material platform is almost uniquely based on III–V compounds, as previously described. On the passive resonator side, we introduce four material platforms that have demonstrated high performance and suitability for commercial applications:

1) InP/InGaAsP resonator [73], [76];
2) Si resonator [77], [78];
3) SiN resonator [74];
4) SiO$_2$ PLC resonator [74].

With the hybrid integration approach, we define the technology used to closely integrate active and passive materials. In contrast to the case of InP compounds, where the homogeneous nature of the active and passive material platform allows the use of traditional InP wafer processing, the cointegration of Si/SiN/SiO$_2$ with InP requires a way to overcome the material differences, especially in terms of lattice constant mismatch. While direct epitaxy of InP compounds on a silicon substrate would potentially simplify the process and reduce the fabrication cost, current demonstrations of this approach do not meet the requirements of commercial devices [79], [80]. Other solutions require some level of die-to-die or die-to-wafer bonding and, in some cases, a few heterogeneous wafer processing steps.

Butt coupling has been extensively utilized to create external cavity lasers with high output power and wide tunability and thin linewidth. With this technology, an InP die with an active gain section waveguide (typically an
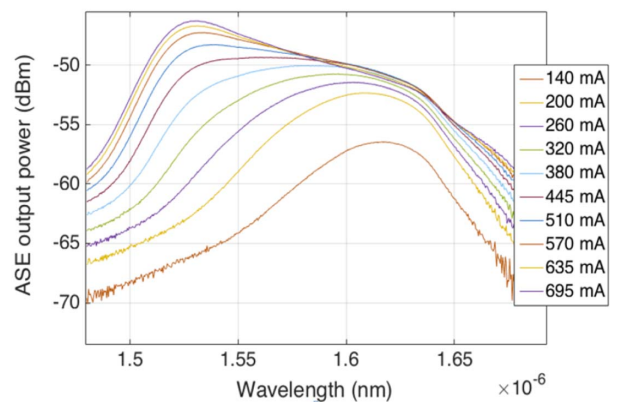

Fig. 12. *Ultrawide RSOA optical gain bandwidth depending on current injected into the RSOA.*

RSOA) is butt coupled to a passive resonator through flip chip [77]. This approach is flexible and can be used with different kinds of passive resonators. It is also quite scalable, allowing for a bar of RSOA to be butt coupled to a passive chip with a bar of resonators. The biggest challenge is how to achieve a low-loss coupling interface between the active waveguide and the passive waveguide. Typically, expanded mode beam couplers have been used to consistently achieve coupling loss below 1 dB.

Die-to-wafer bonding is another approach that has been successfully demonstrated with several flavors. Heterogeneous III–V on silicon die-to-wafer bonding was the first approach utilized to create a hybrid cavity TL [81], [82]. With this approach, unpatterned III–V dies are bonded on a silicon wafer and then processed at the wafer level. Bonding is typically based on Van der Waals forces (molecular bonding) or is enhanced by an adhesive material. The processing includes substrate removal, waveguide patterning, passivation, and metal contact deposition.

The optical coupling between the passive resonator and the active waveguide is obtained through adiabatic coupling, achieving that a very low reflection level from this interface is key as nested cavity behavior can easily deteriorate laser tunability and broaden the linewidth [83].

More recently, heterogeneous integration based on transfer print technology has been proposed [84]. With transfer print, the III–V die is typically much smaller because only individual devices are transferred in general. The die or coupon is at least partially patterned before being bonded to the target wafer, and the fabrication is completed after the transfer print. Depending on the approach, post-bonding fabrication can involve only passivation and metal patterning or also other steps such as III–V etching [85].

Transfer print allows for different coupling configurations between the active and the passive waveguides, and both butt coupling and evanescent coupling have been reported.

D. Intracavity Filter and Wavelength Locking

Once the gain medium has been integrated within the cavity, an intracavity optical filter can be used to achieve a single-mode operation. A phase shifter is usually placed into the cavity, as well as an optical (tunable) filter for the wavelength selection. AWGs, a cascaded MZI, an SGDBR, or ring resonators can be used to fulfill this function. Finally, the cavity is terminated using an integrated mirror if needed (the reflective and filtering functions can be done in one device too, e.g., as for SGDBR). The Fabry–Perot mode of the cavity starts lasing when the gain overcomes the cavity loss and single-mode operation is ensured by attenuating nonlasing FP modes through the filtering function.

Therefore, the material and the design of the external cavity are key parameters to obtain high-performances TLs. An extensive overview of Si/SiN/SiO$_2$ TL linewidths was
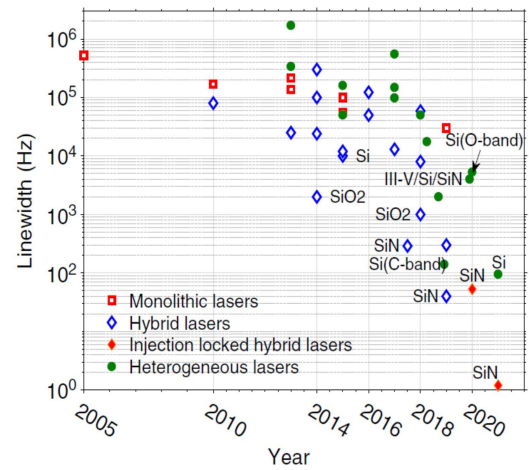

Fig. 13. *Laser linewidths for monolithic, heterogeneously integrated, hybrid, and injection-locked hybrid lasers [86].*

reported [86] and is shown in Fig. 13. SiN- and SiO$_2$-based external cavities offer lower loss, which enables lower linewidth and higher output power. However, overcoming the loss of the silicon cavity remains challenging, and SOA boosters have been used to ensure high output power [87]. To avoid the use of an extra booster SOA, a high-saturation-power SOA can be used, which has exhibited fiber-coupled optical power up to 20 mW (13 dBm) [72]. The fiber-coupled output power is measured depending on the injected current into the RSOA, as shown in Fig. 14. The threshold current is 95 mA and the slope efficiency of the fiber-coupled output power is 5% (W/A).

The large thermo-optic coefficient of silicon allows for a wide range of frequency tunability. However, it also makes the wavelength stabilization challenging. One of the advantages of using SiN or Si materials, which are
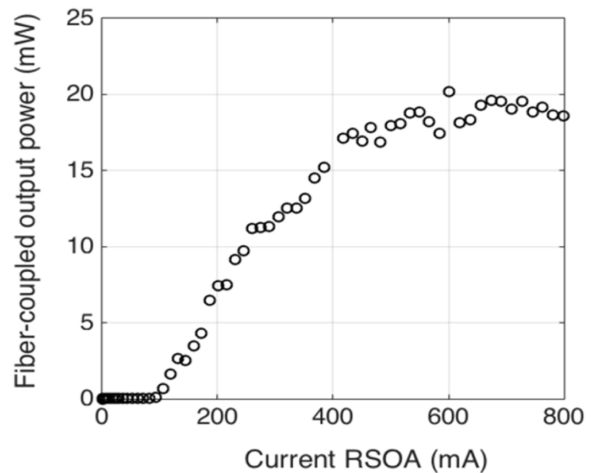

Fig. 14. *Hybrid III–V/Si laser via edge coupling L–I curve as a function of current injected into the RSOA [72].*

compatible with a full silicon-photonic process, is the availability of photodiodes (Ge-based) and pin or p-n junctions (for variable optical attenuation or fast phase shifting), which enable complex cavity designs. Several functionalities have been demonstrated, including controlling the facet reflectivity [88], fast wavelength switching [89], wavelength stabilized lasers [90], and multiwavelength lasers [91]. Locking to a specific grid according to the WDM systems is key to ensure proper multiplexing. Several frequency stabilization methods for silicon microring resonators have been reported using balanced homodyne detection [92] and on-chip temperature monitoring [90]. Recently, an integrated silicon athermal WLL has been proposed for an athermal operation over a temperature range of 40 °C [93]. The WLL is incorporated with a thermo-optic phase shifter that provides tuning of the frequency lock point and dithering of the WLL response without affecting its athermal behavior.

Fig. 15. *Schematic of hybrid III–V/Si wavelength tunable IQ transmitter including one hybrid wavelength TL and two microring modulators nested in an MZI modulator [97].*

E. Toward Laser Integration With Transceiver

As previously discussed, laser integration with the transceiver only makes sense in specific scenarios. Nevertheless, integrating laser diodes with modulators or a coherent receiver has been pursued to develop the next generation of ultracompact transceivers. Several chips can be copackaged in the optoelectronic transmitter. For example, in [94], laser and modulator chips were copackaged and used to generate optical data at rates up to 32 GBd. The first generation of monolithically integrated transmitters was inspired by LiNbO$_3$ MZM and was designed with the InP technology. A monolithic transmitter involving an MZM with a sampled grating-distributed Bragg reflector TL, an SOA, and an absorber was reported, producing data streams at 10 GBd [95]. However, the transmitter was limited to a specific range by the MZM modulation bandwidth. More recently, 14 I-Q MZMs and lasers work together with an external polarization multiplexer to increase the rate of information transfer between the sender and the receiver to up to 44 GBd per laser [96]. To reduce its footprint, the silicon-photonic-based transmitter is a natural candidate, and a hybrid III–V/Si wavelength-tunable transmitter based on ring modulators for advanced modulation format generation has been proposed [97]. The two-arm interferometric structure shown in Fig. 15 was used to generate a QPSK modulation format. To do so, we first generated a BPSK signal using each ring and then assigned a phase difference of $\pi/2$ between the two arms of the interferometer by adjusting the current of the PSs. The 80-Gb/s PDM-QPSK transmission in back-to-back and over 100-km SMF was achieved and the Q^2-factor above the FEC limit was measured even after 100-km transmission.

V. PHOTONIC INTEGRATED CIRCUITS

There is constant pressure to reduce the cost, size, and power consumption per transmitted bit. Historically, this has been accomplished 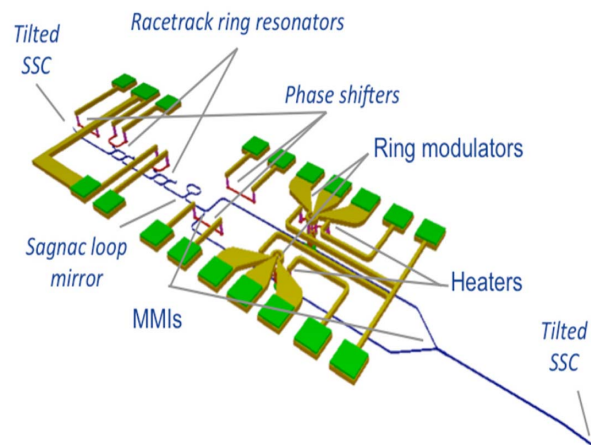by increasing the number of bits per symbol and the transmitted symbol rate. Furthermore, in the past, the cost pressure on optical transceivers was not very high because other costs dominated, such as the fiber plant or electronics. However, severe limits have now been reached on the bits per symbol and the symbol rate, and the cost of optical transceivers is dominating systems. The main way forward is increasing the amount of optical and electronic integration. This integration must be cost-effective and reduce power consumption as well.

There are three main techniques to increase integration: increasing the number of optical ports per subassembly, increasing the number of optical carriers per subassembly, and increasing the subsystem density, as shown in Fig. 16. Increasing the number of optical ports saves on packaging costs, such reducing the total number of fiber-to-chip alignments. However, such integration demands high PIC yields since, otherwise, the cost could actually increase due to yield loss. Increasing the number of optical carriers also saves some packaging costs, but it may require the integration of wavelength multiplexers and demultiplexers, which adds some cost and complexity. Increasing the density will be discussed in Section V-D.

A. Large-Scale Integration

An important consideration of large-scale integration in PICs is yield. If the yield of any component is too low, the cost penalty of the yield loss will outweigh the benefit of the integration. Thus, large-scale integration favors silicon photonics because silicon is a single-element material grown in a liquid (unlike InGaAsP, which is a quaternary material grown in a reactor), and mature silicon processes have been developed by the electronics industry. However, silicon photonics does have an epitaxially grown Ge photodetector [98], which is typically a yield-limiting element. A cross-sectional view of a typical silicon-photonic platform is shown in Fig. 17.
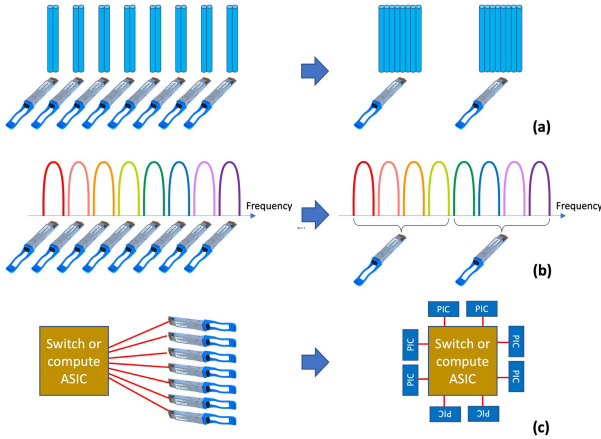
Fig. 16. *Three main techniques to increase integration: (a) increasing the number of optical ports per subassembly, (b) increasing the number of optical carriers per subassembly, and (c) increasing the density.*

Table 2 Silicon-Photonic Element Yield Classes

Element class	Elements	Yield
Non-epitaxial, low dimension sensitivity	Waveguides, modulators, VOAs, polarization splitters / rotators, phase shifters	High
Non-epitaxial, high dimension sensitivity	Grating couplers, directional couplers, MMI couplers, narrow-band filters	Medium
Epitaxial, zero or reverse biased	Photodiodes	Medium-low
Epitaxial, forward biased	Lasers	Low

Silicon-photonic elements can be divided into four main classes, as listed in Table 2. The first class encompasses devices in the crystalline silicon or deposited silicon nitride that is not highly sensitive to waveguide width, thickness, or spacing; an example is optical modulators. The second class encompasses devices in the crystalline silicon or deposited silicon nitride that is highly sensitive to waveguide width, thickness, or spacing, such as grating couplers. The third class encompasses epitaxial devices that are reverse-biased, such as Ge photodiodes. The fourth class encompasses epitaxial materials that are forward-biased, e.g., lasers, which today involve III–V materials. As an example, assume that a coherent PIC has 12 photodiodes per carrier. If each photodiode has a 98% yield, going from one carrier per PIC to four carriers per PIC reduces the capacity per wafer by a factor of 2. Thus, to support large-scale integration, the yield of even the medium-low-yield elements must be significantly better than 99%.

B. Multiport Connections

As mentioned, one way to increase integration is increasing the number of optical connections per PIC. A first step is placing the coherent transmitter and receiver on the same die, as demonstrated in [99]. This reduces the number of fiber connections, fiber alignments, and external components.
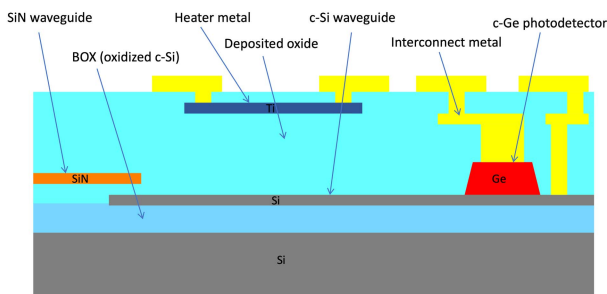
The above considers separate fibers as the multiple inputs. However, to increase both optical input–output density and transport density, we can use fibers with multiple cores and/or a core that guide multiple spatial modes. Close spacing of cores or multimode cores offers the highest density but requires MIMO demultiplexing due to unpredictable amounts of mutual coupling. MIMO demultiplexing can be done electronically or optically. Electronic demultiplexing is currently faster and more robust but consumes significantly more power.

Photonic integration is well suited for optical coupling to the dense modes because we can couple through the surface of the PIC with precise patterns by using grating couplers [100]. Doerr and Taunay [101] demonstrated 14 IM-DD receivers on a single die coupled via a seven-core fiber and Doerr et al. [102] demonstrated coupling to multiple modes of a ring-core fiber, both using silicon grating couplers. Fig. 18 shows the circular grating coupler used to couple to the ring-core fiber.

Photonic integration is also well suited for optical MIMO demultiplexing. Doerr et al. [103] and Fontaine et al. [104] demonstrated optical MIMO demultiplexing of two and six modes, respectively. The main challenge in optical MIMO demultiplexing is making it "endless," i.e., not having any optical phase shifters run out of range while trying to take an arbitrarily evolving signal.

C. Multiwavelength Transceivers

Fig. 19 shows a compact example that integrates four coherent receivers in one die, using a chirped

Fig. 17. *Cross section of a typical silicon-photonics platform.*
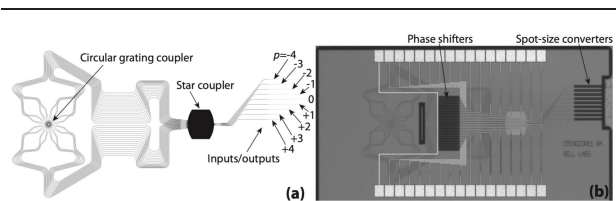

Fig. 18. *PIC that couples to multiple modes of a ring-core fiber. The fiber is placed normal to the PIC, at the center of the circular grating coupler.*
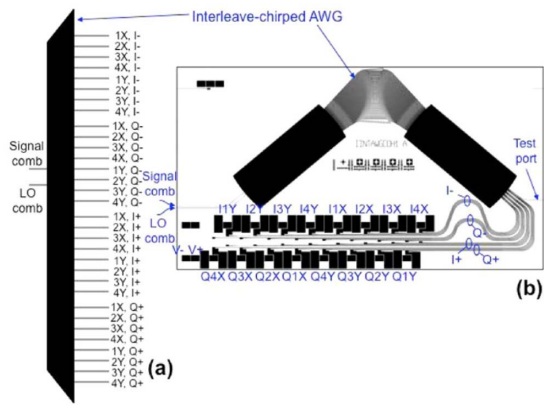
Fig. 19. *Four-wavelength, dual-polarization, dual-quadrature coherent receiver.*

Fig. 21. *(a) Separate packages and (b) CPO.*

arrayed-waveguide grating as a wavelength demultiplexer for both signal and LO, as a polarization demultiplexer, and as a 90° hybrid [105]. While this demonstration was in InP, it could be made in silicon as well.

The modulator and receiver PIC are not the only optical element that can save size, cost, and power by integrating multiple carriers. The laser can integrate multiple channels as well, as shown in Fig. 20(a). Fig. 20(b) shows an example design of a multichannel TL, in which one SOA provides the gain for multiple TLs integrated on a single silicon-photonics die. Fig. 20(c) shows the laser output, which has independent tuning of two wavelengths [106]. Such a design is especially suitable for coherent transceivers, in which it is advantageous to have the laser separate from the rest of the optics and electronics.

An optical isolator is generally required at the output of the narrow-linewidth laser; otherwise, reflections back into the laser, depending on their relative phase, can cause linewidth broadening and/or mode hopping. If the reflection phase is randomly varying, the reflections can also cause significant relative intensity noise (RIN). This isolator is usually made of bulk optics and is integrated inside the TL output coupler. Ideally, this isolator is on the thermoelectric cooler of the laser, so it can maintain high isolation over the allowable case temperature range.
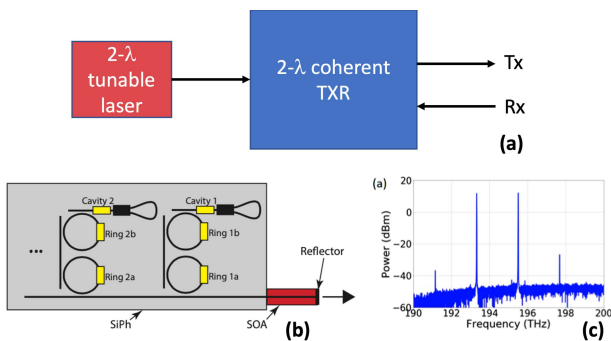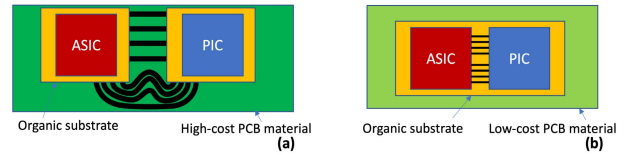
If the laser is integrated with the transmitter PIC, it may be possible to move the isolator to the transmitter output, provided that the transmitter PIC return loss is greater than ~40 dB. The isolator is still necessary in this case because there may be back reflections from the transmission fiber. The one exception in which an isolator for a laser can be completely avoided is that if the laser is only for the LO, the receiver PIC return loss is greater than ~40 dB. Isolators are not required anywhere else in the coherent transceiver, unless the PIC return loss is less than ~30 dB, in which case typical standards for transceiver return loss cannot be met.

D. Copackaged Optics

In CPO, the ASIC that needs the I/O and the optics supplying the I/O is placed on the same substrate. The substrate is an organic or ceramic circuit board with high-resolution lithography (typically 50 μm), as opposed to a glass-fiber-based PCB with low-resolution lithography (typically 125 μm). Fig. 21 shows the drawings of the standard case of separate packages and the CPO case. As we can see, the CPO case results in a smaller size, lower cost, lower skews, lower RF losses, and shorter return times of RF reflections. The latter allows for fewer equalization taps. As with all integrations, the advantages of CPO will be negated if the yield is low.

With coherent CPO, it is advantageous to keep the laser separate from the CPO assembly because the CPO has a large, dense heat dissipation, and the laser yield is too low to risk throwing away the entire CPO if the laser fails. However, there are some CPO architectures that contain integrated lasers, and these have redundant lasers to mitigate the risk [107].
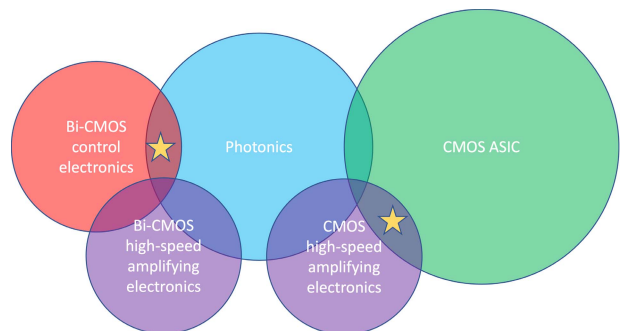

Fig. 20. *Multichannel TL feeding a multicarrier PIC.*

Fig. 22. *Options for monolithic integration of photonics and electronics.*
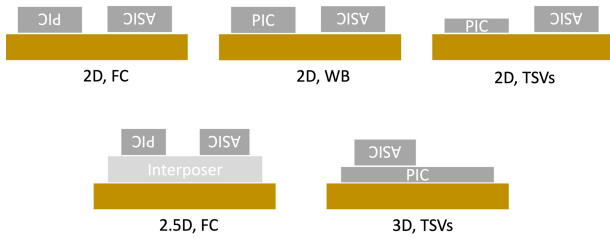
Fig. 23. *Various packing configurations for CPO. FC = flip chip, WB = wire-bond, TSV = through-silicon-via.*

The CPO contains some electronic elements not shown in Fig. 21, including drivers, TIAs, and controls. These can be separate chips, or they can be monolithically integrated to further reduce the cost, size, and power consumption. Fig. 22 shows the main components, and overlapping regions indicate opportunities for monolithic integration. The starred regions show monolithic integration with exceptional promise. For example, integrating the driver and TIAs into the main CMOS ASIC can significantly reduce power consumption.

There are many variations in how the CPO is built. Fig. 23 shows some possible configurations, ranging from 2-D, where the PIC and ASIC are side-by-side to 3-D, where one chip is on top of another. An example of a flip-chip coherent PIC was demonstrated in [108].

A significant drawback to coherent link is that, unlike an IM-DD SERDES, a coherent SERDES is only for optics and cannot drive an electrical cable efficiently. One reason is for this is that a coherent link generally requires oversampling in the receiver, while an IM-DD link does not. For example, with PAM4, the exact same electronics can drive an electrical cable with PAM4 or an optical link with PAM4. This allows large ASICs to have just one SERDES that does both electrical and optical, as shown in Fig. 24. Thus, it is unlikely that a coherent link will be possible for CPO with large ASICs in the near future. Instead, we will focus on CPO with small ASICs.

E. Integrated Optical Gain

As the number of channels per PIC increases, insertion losses increase due to more power splitting and the presence of wavelength multiplexers and demultiplexers. Consequently, the potential benefit of integrated optical
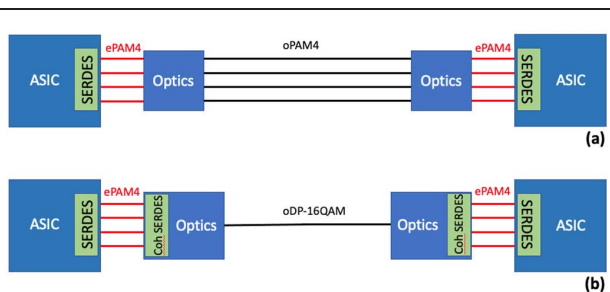

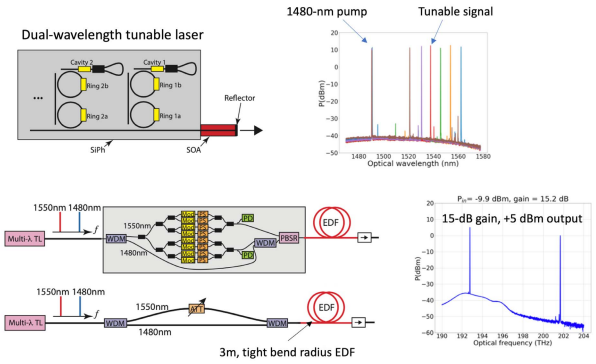**Fig. 24.** *Diagram showing (a) IM-DD link and (b) coherent link.*

Fig. 25. *Integrated optical gain using a dual-TL and a short piece of Er-doped fiber.*

gain increases significantly with increased integration. For coherent link, it is important that the optical gain has low nonlinearity and low polarization dependence. A good choice is EDFA. The cost of an EDFA can be reduced by integrating the pump laser into the signal-source laser. Fig. 25 shows an example, where a dual TL is utilized in which one of the wavelengths is a 1480-nm pump laser for the EDFA [109].

VI. CONCLUSION

In this article, we presented the recent progress on optical coherent transceiver technology and the challenges involved in scaling it up to massive parallelization in SDM transmission systems. We presented theoretical capacity limits under the presence of MDL in SDM systems and then discussed the DSP chain for SDM transmission systems with a wide time-dispersive channel due to DGD between spatial modes, along with the challenges for implementing an ASIC chip. We presented laser source technologies for filling wavelengths in the spatial channels in SDM systems and discussed integrated III–V and hybrid III–V/SOI/SiN TLs that can simultaneously offer tunability, narrow linewidth, low power consumption, and compactness. We presented PIC technologies to achieve small-size, cost-effective, low power consumption transceivers for massive parallelized SDM transmission systems. We also discussed the challenges and prospects of a silicon-photonic platform for large-scale integration of key elements of the transceiver, such as modulators, and photodiodes and CPO for connecting PIC to a DSP ASIC chip.

It has been challenging to energy-efficiently increase the aggregate net data rate of SMF-based WDM transmission systems to the peta-bit-class capacity as digital coherent transceiver technologies mature and offer flexible functions. SDM is an attractive approach to meet the continuous-growth traffic demands. However, to realize deployable SDM transmission systems, we need to address many technical challenges on the elements such as SDM fibers/cables, inline optical amplifiers, MIMO DSP ASICs,

laser sources, and PICs, as well as establish the design of SDM transmission systems. If the research and development on these technical issues dramatically progresses in the next few years, SDM will be a promising solution for the next few decades. We expect the continuous development of the highly integrated optical transceiver technologies presented in this article, as well as other SDM elements such as optical nodes, new fibers, and technologies for connecting them. ∎

REFERENCES

[1] T. Kawasaki et al., "Development of 100-Gbit/s packet transport system," *NTT Tech. Rev.*, vol. 13, no. 3, Mar. 2015.

[2] K. Kikuchi, "Fundamentals of coherent optical fiber communications," *J. Lightw. Technol.*, vol. 34, no. 1, pp. 157–179, Jun. 1, 2016.

[3] S. J. Savory, "Digital filters for coherent optical receivers," *Opt. Exp.*, vol. 16, no. 2, pp. 804–817, Jan. 2008.

[4] H. Zhang et al., "200 Gb/s and dual-wavelength 400 Gb/s transmission over transpacific distance at 6 b/s/Hz spectral efficiency," in *Proc. Opt. Fiber Commun. Conf. (OFC)*, Mar. 2013, pp. 1–3.

[5] M. Salsi et al., "38.75 Tb/s transmission experiment over transoceanic distance," in *Proc. 39th Eur. Conf. Exhib. Opt. Commun. (ECOC)*, Sep. 2013, pp. 1–3.

[6] F. Yaman et al., "First quasi-single-mode transmission over transoceanic distance using few-mode fibers," in *Proc. Opt. Fiber Commun. Conf. (OFC)*, Mar. 2015, pp. 1–3.

[7] S. Zhang et al., "Capacity-approaching transmission over 6375 km using hybrid quasi-single-mode fiber spans," *J. Lightw. Technol.*, vol. 35, no. 3, pp. 481–487, Feb. 1, 2017.

[8] A. Ghazisaeidi et al., "65Tb/s transoceanic transmission using probabilistically-shaped PDM-64QAM," in *Proc. ECOC*, Sep. 2016, pp. 1–3.

[9] J.-X. Cai et al., "70.4 Tb/s capacity over 7,600 km in C+L band using coded modulation with hybrid constellation shaping and nonlinearity compensation," in *Proc. Opt. Fiber Commun. Conf. Postdeadline Papers*, Mar. 2017, pp. 1–3.

[10] M. Ionescu et al., "74.38 Tb/s transmission over 6300 km single mode fiber with hybrid EDFA/Raman amplifiers," in *Proc. Opt. Fiber Commun. Conf. (OFC)*, Mar. 2019, pp. 1–3.

[11] C. E. Shannon, "A mathematical theory of communication," *Bell Syst. Tech. J.*, vol. 27, no. 3, pp. 379–423, Oct. 1948.

[12] F. Hamaoka et al., "Ultra-wideband WDM transmission in S-, C-, and L-bands using signal power optimization scheme," *J. Lightw. Technol.*, vol. 37, no. 8, pp. 1764–1771, Apr. 15, 2019.

[13] L. Galdino et al., "Optical fibre capacity optimisation via continuous bandwidth amplification and geometric shaping," *IEEE Photon. Technol. Lett.*, vol. 32, no. 17, pp. 1021–1024, Sep. 1, 2020.

[14] K. Takenaga, S. Omori, R. Goto, S. Tanigawa, S. Matsuo, and K. Himeno, "Evaluation of high-power endurance of bend-insensitive fibers," in *Proc. OFC*, Feb. 2008, pp. 1–3.

[15] T. Morioka, Y. Awaji, R. Ryf, P. Winzer, D. Richardson, and F. Poletti, "Enhancing optical communications with brand new fibers," *IEEE Commun. Mag.*, vol. 50, no. 2, pp. s31–s42, Feb. 2012, doi: 10.1109/MCOM.2012.6146483.

[16] H. Takara et al., "1.01-Pb/s (12 SDM/222 WDM/456 Gb/s) crosstalk-managed transmission with 91.4-b/s/Hz aggregate spectral efficiency," in *Proc. Eur. Conf. Exhib. Opt. Commun.*, Sep. 2012, pp. 1–3.

[17] D. Qian et al., "1.05Pb/s transmission with 109b/s/Hz spectral efficiency using hybrid single- and few-mode cores," in *Proc. FIO*, Oct. 2012, pp. 1–2.

[18] D. Soma et al., "2.05 peta-bit/s super-Nyquist-WDM SDM transmission using 9.8-km 6-mode 19-core fiber in full C band," in *Proc. Eur. Conf. Opt. Commun. (ECOC)*, Sep. 2015, pp. 1–3.

[19] B. J. Puttnam et al., "2.15 Pb/s transmission using a 22 core homogeneous single-mode multi-core fiber and wideband optical comb," in *Proc. Eur. Conf. Opt. Commun. (ECOC)*, Sep. 2015, pp. 1–3.

[20] T. Kobayashi et al., "1-Pb/s (32 SDM/46 WDM/768 Gb/s) C-band dense SDM transmission over 205.6-km of single-mode heterogeneous multi-core fiber using 96-Gbaud PDM-16QAM channels," in *Proc. OFC*, Mar. 2017, pp. 1–3.

[21] D. Soma et al., "10.16 peta-bit/s dense SDM/WDM transmission over low-DMD 6-mode 19-core fibre across C+L band," in *Proc. Eur. Conf. Opt. Commun. (ECOC)*, Sep. 2017, pp. 1–3.

[22] Y. Loussouarn, E. Pincemin, Y. Pan, G. Miller, A. Gibbemeyer, and B. Mikkelsen, "Multi-rate multi-format CFP/CFP₂ digital coherent interfaces for data center interconnects, metro, and long-haul optical communications," *J. Lightw. Technol.*, vol. 37, no. 2, pp. 538–547, Jan. 15, 2019, doi: 10.1109/JLT.2018.2875249.

[23] F.-W. Sun and H. C. A. van Tilborg, "Approaching capacity by equiprobable signaling on the Gaussian channel," *IEEE Trans. Inf. Theory*, vol. 39, no. 5, pp. 1714–1716, Sep. 1993.

[24] I. B. Djordjevic, H. G. Batshon, L. Xu, and T. Wang, "Coded polarization-multiplexed iterative polar modulation (PM-IPM) for beyond 400 Gb/s serial optical transmission," in *Proc. Opt. Fiber Commun. Conf.*, Mar. 2010, pp. 1–3.

[25] F. Buchali, F. Steiner, G. Böcherer, L. Schmalen, P. Schulte, and W. Idler, "Rate adaptation and reach increase by probabilistically shaped 64-QAM: An experimental demonstration," *J. Lightw. Technol.*, vol. 34, no. 7, pp. 1599–1609, Apr. 2016.

[26] P. W. Berenguer et al., "Nonlinear digital pre-distortion of transmitter components," *J. Lightw. Technol.*, vol. 34, no. 8, pp. 1739–1745, Apr. 15, 2016.

[27] R. Kudo, T. Kobayashi, K. Ishihara, Y. Takatori, A. Sano, and Y. Miyamoto, "Coherent optical single carrier transmission using overlap frequency domain equalization for long-haul optical systems," *J. Lightw. Technol.*, vol. 27, no. 16, pp. 3721–3728, Aug. 15, 2009.

[28] *Optical Monitoring for Dense Wavelength Division Multiplexing Systems*, document (ITU-T), Rec. G.697, International Telecommunication Union Telecommunication Standardization, Nov. 2016.

[29] E. Yamazaki et al., "Fast optical channel recovery in field demonstration of 100-Gbit/s Ethernet over OTN using real-time DSP," *Opt. Exp.*, vol. 19, pp. 13179–13184, Jul. 2011.

[30] B. Lavigne et al., "400 Gb/s real-time trials on commercial systems for next generation networks," *J. Lightw. Technol.*, vol. 34, no. 2, pp. 477–483, Jan. 15, 2016, doi: 10.1109/JLT.2015.2476697.

[31] H. Zhang et al., "Real-time transmission of single-carrier 400 Gb/s and 600 Gb/s 64QAM over 200km-span link," in *Proc. 45th Eur. Conf. Opt. Commun. (ECOC)*, Sep. 2019, pp. 1–3, doi: 10.1049/cp.2019.0846.

[32] Y. R. Zhou et al., "Field and laboratory demonstration of real-time 1.2T (2×600G) over G.652/G.654.E fiber distances up to 100km with net spectral efficiency up to 8bit/s/Hz," in *Proc. Asia Commun. Photon. Conf. (ACPC)*, Nov. 2019, pp. 1–3.

[33] F. Hamaoka et al., "Dual-carrier 1-Tb/s transmission over field-installed G.654.E fiber link using real-time transponder," *IEICE Trans. Commun.*, vol. E103-B, no. 11, pp. 1–7, 2020.

[34] H. Sun et al., "800G DSP ASIC design using probabilistic shaping and digital sub-carrier multiplexing," *J. Lightw. Technol.*, vol. 38, no. 17, pp. 4744–4756, Sep. 1, 2020.

[35] A. Alvarado, E. Agrell, D. Lavery, R. Maher, and P. Bayvel, "Replacing the soft-decision FEC limit paradigm in the design of optical communication systems," *J. Lightw. Technol.*, vol. 33, no. 20, pp. 4338–4352, Oct. 15, 2015.

[36] J. Cho and P. J. Winzer, "Probabilistic constellation shaping for optical fiber communications," *J. Lightw. Technol.*, vol. 37, no. 6, pp. 1590–1607, Mar. 15, 2019.

[37] J. Cho, X. Chen, S. Chandrasekhar, and P. Winzer, "On line rates, information rates, and spectral efficiencies in probabilistically shaped QAM systems," *Opt. Exp.*, vol. 26, pp. 9784–9791, Apr. 2018.

[38] T. Kawasaki et al., "Development of beyond 100G optical cross connect (B100G-OXC) system," *NTT Tech. Rev.*, vol. 19, no. 11, pp. 59–64, 2021.

[39] Y. Ogiso et al., "Ultra-high bandwidth InP IQ modulator co-assembled with driver IC for beyond 100-GBd CDM," in *Proc. Opt. Fiber Commun. Conf. Postdeadline Papers*, Mar. 2018, pp. 1–3.

[40] M. Zhang et al., "Ultra-high bandwidth integrated lithium niobate modulators with record-low V_π," in *Proc. Opt. Fiber Commun. Conf. Postdeadline Papers*, Mar. 2018, pp. 1–3.

[41] T. Jyo et al., "A 241-GHz-bandwidth distributed amplifier with 10-dBm P1dB in 0.25-μm InP DHBT technology," in *Proc. IMS*, Jun. 2019, pp. 1430–1433.

[42] Keysight Technologies. (Jul. 2018). *Infiniium UXR-Series Oscilloscopes*. [Online]. Available: https://www.keysight.com/us/en/products/oscilloscopes/infiniium-real-time-oscilloscopes/infiniium-uxr-series-oscilloscopes.html

[43] T. Drenski and J. C. Rasmussen, "ADC/DAC and ASIC technology trends," in *Proc. OECC/PSC*, Jul. 2019, pp. 1–3.

[44] X. Chen et al., "All-electronic 100-GHz bandwidth digital-to-analog converter generating PAM signals up to 190 GBaud," *J. Lightw. Technol.*, vol. 35, no. 3, pp. 411–417, Feb. 1, 2017.

[45] H. Yamazaki et al., "Digital-preprocessed analog-multiplexed DAC for ultrawideband multilevel transmitter," *J. Lightw. Technol.*, vol. 34, no. 7, pp. 1579–1584, Apr. 1, 2016.

[46] *Series G: Transmission Systems and Media, Digital Systems and Networks*, document (ITU-T), G-series Recommendations Supplement 39, Ed5, International Telecommunication Union Telecommunication Standardization, 2016.

[47] Y. Sasaki, K. Takenaga, K. Aikawa, Y. Miyamoto, and T. Morioka, "Single-mode 37-core fiber with a cladding diameter of 248 μm," in *Proc. Opt. Fiber Commun. Conf.*, Mar. 2017, pp. 1–3.

[48] R. Ryf et al., "MIMO-based crosstalk suppression in spatially multiplexed 3×56-Gb/s PDM-QPSK signals for strongly coupled three-core fiber," *IEEE Photon. Technol. Lett.*, vol. 23, no. 20, pp. 1469–1471, Oct. 2011.

[49] N. K. Fontaine et al., "30×30 MIMO transmission over 15 spatial modes," in *Proc. Opt. Fiber Commun. Conf. Post Deadline Papers*, Mar. 2015, pp. 1–3.

[50] T. Hayashi et al., "6-mode 19-core fiber for weakly-coupled mode-multiplexed transmission over uncoupled cores," in *Proc. Opt. Fiber Commun. Conf.*, Mar. 2016, pp. 1–3.

[51] T. Sakamoto et al., "Low-loss and low-DMD few-mode multi-core fiber with highest core multiplicity factor," in *Proc. OFC*, Mar. 2016, pp. 1–3.

[52] D. Tse and P. Viswanath, *Fundamentals of Wireless Communication*. New York, NY, USA: Cambridge Univ. Press, 2005.

[53] K.-P Ho and J. M. Kahn, "Mode-dependent loss and gain: Statistics and effect on mode-division multiplexing," *Opt. Exp.*, vol. 19, no. 17, pp. 16612–16635, 2011.

[54] G. Rademacher et al., "High capacity transmission with few-mode fibers," *J. Lightw. Technol.*, vol. 37, no. 2, pp. 425–432, Jan. 2019.

[55] G. Rademacher et al., "Long-haul transmission over few-mode fibers with space-division multiplexing," *J. Lightw. Technol.*, vol. 36, no. 6, pp. 1382–1388, Mar. 15, 2018.

[56] C. Antonelli, M. Shtaif, and A. Mecozzi, "Modeling of nonlinear propagation in space-division multiplexed fiber-optic transmission," *J. Lightw. Technol.*, vol. 34, no. 1, pp. 36–54, Jan. 1, 2016, doi: 10.1109/JLT.2015.2510511.

[57] R. Ryf et al., "Long-haul transmission over multi-core fibers with coupled cores," in *Proc. Eur. Conf. Opt. Commun. (ECOC)*, Sep. 2017, pp. 1–3.

[58] A. Mecozzi, C. B. Clausen, and M. Shtaif, "Analysis of intrachannel nonlinear effects in highly dispersed optical pulse transmission," *IEEE Photon. Technol. Lett.*, vol. 12, no. 4, pp. 392–394, Apr. 2000.

[59] J. Cho, "Balancing probabilistic shaping and forward error correction for optimal system performance," in *Proc. OFC*, Mar. 2018, pp. 1–3.

[60] N. Gisin, R. Passy, and J. P von der Weid, "Definitions and measurements of polarization mode dispersion: Interferometric versus fixed analyzer methods," *IEEE Photon. Technol. Lett.*, vol. 6, no. 6, pp. 730–732, Jun. 1994.

[61] S. Ö. Arik, D. Askarov, and J. M. Kahn, "Effect of mode coupling on signal processing complexity in mode-division multiplexing," *J. Lightw. Technol.*, vol. 31, no. 3, pp. 423–431, Feb. 2013.

[62] T. Hayashi, Y. Tamura, T. Hasegawa, and T. Taru, "Record-low spatial mode dispersion and ultra-low loss coupled multi-core fiber for ultra-long-haul transmission," *J. Lightw. Technol.*, vol. 35, no. 3, pp. 450–457, Feb. 1, 2017.

[63] C. Antonelli, A. Mecozzi, M. Shtaif, and P. J. Winzer, "Stokes-space analysis of modal dispersion in fibers with multiple mode transmission," *Opt. Exp.*, vol. 20, no. 11, pp. 11718–11733, 2012.

[64] O. Zia-Chahabi, R. L. Bidan, M. Morvan, and C. Laot, "Efficient frequency-domain implementation of block-LMS/CMA fractionally spaced equalization for coherent optical communications," *IEEE Photon. Technol. Lett.*, vol. 23, no. 22, pp. 1697–1699, Nov. 2011.

[65] K. Shibahara et al., "Dense SDM (12-core x 3-mode) transmission over 527 km with 33.2-ns mode-dispersion employing low-complexity parallel MIMO frequency-domain equalization," *J. Lightw. Technol.*, vol. 34, no. 1, pp. 196–204, Jan. 1, 2016, doi: 10.1109/JLT.2015.2463102.

[66] K. P. Ho and J. M. Kahn, "Mode coupling and its impact on spatially multiplexed systems," in *Optical Fiber Telecommunications VIB: Systems and Networks*. Waltham, MA, USA: Academic, 2013.

[67] P. J. Winzer and G. J. Foschini, "MIMO capacities and outage probabilities in spatially multiplexed optical transport systems," *Opt. Exp.*, vol. 19, no. 17, pp. 16680–16696, Aug. 2011.

[68] M. D. Feuer et al., "Joint digital signal processing receivers for spatial superchannels," *IEEE Photon. Technol. Lett.*, vol. 24, no. 21, pp. 1957–1960, Oct. 2012.

[69] G. de Valicourt et al., "80Gb/s PDM-QPSK PIC-to-PIC transmission based on integrated hybrid silicon/III–V wavelength-tunable transmitter and monolithic silicon coherent receiver," in *Proc. OFC*, Mar. 2017, pp. 1–3.

[70] A. Fallahpour et al., "Demonstration of wavelength tunable optical modulation format conversion from 20 and 30 gbit/s qpsk to pam4 using nonlinear wave mixing," *Opt. Commun.*, vol. 459, Mar. 2020, Art. no. 124871.

[71] S. Namiki and Y. Emori, "Ultrabroad-band Raman amplifiers pumped and gain-equalized by wavelength-division-multiplexed high-power laser diodes," *IEEE J. Sel. Topics Quantum Electron.*, vol. 7, no. 1, pp. 3–16, Jan. 2001.

[72] G. de Valicourt et al., "Integrated ultra-wide band wavelength-tunable hybrid external cavity silicon-based laser," in *Proc. OFC*, Mar. 2017, pp. 1–3.

[73] H. Ishii, H. Tanobe, F. Kano, Y. Tohmori, Y. Kondo, and Y. Yoshikuni, "Quasicontinuous wavelength tuning in super-structure-grating (SSG) DBR lasers," *IEEE J. Quantum Electron.*, vol. 32, no. 3, pp. 433–441, Mar. 1996.

[74] Y. Lin et al., "Characterization of hybrid InP-TriPleX photonic integrated tunable lasers based on silicon nitride (Si_3N_4/SiO_2) microring resonators for optical coherent system," *IEEE Photon. J.*, vol. 10, no. 3, pp. 1–8, Jun. 2018.

[75] H. Debregeas et al., "2 kHz linewidth C-band tunable laser by hybrid integration of reflective SOA and SiO_2 PLC external cavity," in *Proc. Int. Semiconductor Laser Conf.*, Sep. 2014, pp. 50–51.

[76] T. Segawa, S. Matsuo, T. Kakitsuka, T. Sato, Y. Kondo, and R. Takahashi, "Semiconductor double-ring-resonator-coupled tunable laser for wavelength routing," *IEEE J. Quantum Electron.*, vol. 45, no. 7, pp. 892–899, Jul. 2009.

[77] N. Fujioka, T. Chu, and M. Ishizaka, "Compact and low power consumption hybrid integrated wavelength tunable laser module using silicon waveguide resonators," *J. Lightw. Technol.*, vol. 28, no. 21, pp. 3115–3120, Nov. 1, 2010.

[78] G. de Valicourt et al., "Novel bidirectional reflective semiconductor optical amplifier," in *Proc. OECC/PS*, Jul. 2016, pp. 1–3.

[79] J. C. Norman et al., "The importance of p-doping for quantum dot laser on silicon performance," *IEEE J. Quantum Electron.*, vol. 55, no. 2, pp. 1–11, Apr. 2019.

[80] Y. Wan et al., "1.3 μM tunable quantum dot lasers," in *Proc. Conf. Lasers Electro-Opt. (CLEO)*, 2020, Paper SF2E.1.

[81] A. W. Fang et al., "Hybrid silicon evanescent devices," *Mater. Today*, vol. 10, nos. 7–8, pp. 28–35, Jul./Aug. 2007.

[82] G. Roelkens, "III–V/Si photonics by die-to-wafer bonding," *Mater. Today*, vol. 10, nos. 7–8, pp. 36–43, 2007.

[83] G.-H. Duan, "Hybrid III–V on silicon lasers for photonic integrated circuits on silicon," *IEEE J. Sel. Topics Quantum Electron.*, vol. 20, no. 4, pp. 158–170, Jul./Aug. 2014.

[84] J. Juvert et al., "Integration of etched facet, electrically pumped, C-band Fabry–Pérot lasers on a silicon photonic integrated circuit by transfer printing," *Opt. Exp.*, vol. 26, no. 17, pp. 21443–21454, 2018.

[85] C. O. D. Beeck et al., "Heterogeneous III–V on silicon nitride amplifiers and lasers via microtransfer printing," *Optica*, vol. 7, no. 5, pp. 386–393, 2020.

[86] M. A. Tran, D. Huang, and J. E. Bowers, "Tutorial on narrow linewidth tunable semiconductor lasers using Si/III–V heterogeneous integration," *APL Photon.*, vol. 4, no. 11, Nov. 2019, Art. no. 111101.

[87] K. Sato et al., "High output power and narrow linewidth silicon photonic hybrid ring-filter external cavity wavelength tunable lasers," in *Proc. ECOC*, Sep. 2014, pp. 1–3.

[88] G. de Valicourt et al., "Hybrid-integrated wavelength and reflectivity tunable III–V/silicon transmitter," *J. Lightw. Technol.*, vol. 35, no. 8, pp. 1376–1382, Feb. 8, 2017.

[89] G. de Valicourt et al., "Dual hybrid silicon-photonic laser with fast wavelength tuning," in *Proc. OFC*, Mar. 2016, pp. 1–3.

[90] A. Melikyan et al., "Wavelength stabilized silicon/III–V hybrid laser," in *Proc. ECOC*, Sep. 2016, pp. 1–3.

[91] M. S. Eggleston et al., "Simultaneous two-wavelength hybrid III/V-Si laser based on single-section quantum dot gain," in *Proc. ECOC*, Sep. 2016, pp. 1–3.

[92] J. A. Cox, A. L. Lentine, D. C. Trotter, and A. L. Starbuck, "Control of integrated micro-resonator wavelength via balanced homodyne locking," *Opt. Exp.*, vol. 22, no. 9, pp. 11279–11289, 2014.

[93] A. Melikyan, G. de Valicourt, K. Kim, N. Fontaine, Y.-K. Chen, and P. Dong, "Hybrid III–V/silicon laser with integrated athermal wavelength locker," in *Proc. Eur. Conf. Opt. Commun. (ECOC)*, Sep. 2017, pp. 1–3.

[94] S. Chandrasekhar et al., "Small-form-factor all-InP integrated laser vector modulator enables the generation and transmission of 256-Gb/s PDM-16QAM modulation format," in *Proc. OFC*, Mar. 2013, pp. 1–3.

[95] S. B. Estrella, L. A. Johansson, M. L. Masanovic, J. A. Thomas, and J. S. Barton, "First monolithic widely tunable photonic coherent transmitter in InP," *IEEE Photon. Technol. Lett.*, vol. 25, no. 7, pp. 641–643, Apr. 2013.

[96] V. Lal et al., "Full C-band tunable coherent transmitter and receiver InP photonic integrated circuits," in *Proc. ECOC*, Sep. 2016, pp. 1–3.

[97] G. de Valicourt et al., "Integrated hybrid wavelength-tunable III–V/silicon transmitter based on a ring-assisted Mach–Zehnder interferometer modulator," *J. Lightw. Technol.*, vol. 36, no. 2, pp. 204–209, Jan. 15, 2018.

[98] D. Ahn et al., "High performance, waveguide integrated Ge photodetectors," *Opt. Exp.*, vol. 15, no. 7, pp. 3916–3921, Apr. 2007.

[99] C. Doerr et al., "Single-chip silicon photonics 100-Gb/s coherent transceiver," in *Proc. OFC*, Mar. 2014, pp. 1–3.

[100] R. Waldhäusl, B. Schnabel, P. Dannberg, E.-B. Kley, A. Bräuer, and W. Karthe, "Efficient coupling into polymer waveguides by gratings," *Appl. Opt.*, vol. 36, no. 36, pp. 9383–9390, Dec. 1997.

[101] C. R. Doerr and T. F. Taunay, "Silicon photonics core-, wavelength-, and polarization-diversity receiver," *IEEE Photon. Technol. Lett.*, vol. 23, no. 9, pp. 597–599, May 2011.

[102] C. R. Doerr, N. K. Fontaine, M. Hirano, T. Sasaki, L. L. Buhl, and P. J. Winzer, "Silicon photonic integrated circuit for coupling to a ring-core multimode fiber for space-division multiplexing," in *Proc. 37th Eur. Conf. Expo. Opt. Commun.*, Sep. 2011, pp. 1–3.

[103] C. R. Doerr, N. K. Fontaine, and L. L. Buhl, "PDM-DQPSK silicon receiver with integrated monitor and minimum number of controls," *IEEE Photon. Technol. Lett.*, vol. 24, no. 8, pp. 697–699, Apr. 15, 2012.

[104] N. Fontaine et al., "Space-division multiplexing and all-optical MIMO demultiplexing using a photonic integrated circuit," in *Proc. OFC/NFOEC*, Mar. 2012, pp. 1–3.

[105] C. R. Doerr, L. Zhang, and P. J. Winzer, "Monolithic InP multiwavelength coherent receiver using a chirped arrayed waveguide grating," *J. Lightw. Technol.*, vol. 29, no. 4, pp. 536–541, Feb. 15, 2011.

[106] X. Huang et al., "Silicon-photonic laser emitting tunable dual wavelengths with highly correlated phase noise," *Opt. Lett.*, vol. 46, pp. 142–145, Jan. 2021.

[107] S. Fathololoumi et al., "1.6 Tbps silicon photonics integrated circuit for co-packaged optical-IO switch applications," in *Proc. OFC*, Mar. 2020, pp. 1–3.

[108] C. Doerr et al., "Silicon photonics coherent transceiver in a ball-grid array package," in *Proc. OFC*, Mar. 2017, pp. 1–3.

[109] C. R. Doerr et al., "Silicon-photonics multi-wavelength common-gain tunable laser providing both source and pump for an amplified transceiver," *Opt. Lett.*, vol. 46, pp. 625–628, Feb. 2021.

ABOUT THE AUTHORS

Takayuki Kobayashi (Member, IEEE) received the B.E., M.E., and Dr.Eng. degrees from Waseda University, Tokyo, Japan, in 2004, 2006, and 2019, respectively.

In April 2006, he joined NTT Network Innovation Laboratories, Yokosuka, Japan, where he was engaged in research on high-speed and high-capacity digital coherent transmission systems. In April 2014, he moved to NTT Access Network Service Systems Laboratories and engaged in 5G mobile optical network systems. In July 2016, he moved back to NTT Network Innovation Laboratories and has been working on high-capacity optical transmission systems. His current research interests are long-haul optical transmission systems employing spectrally efficient modulation formats enhanced by digital and optical signal processing.

Dr. Kobayashi is a member of the Institute of Electronics, Information and Communication Engineers (IEICE) of Japan and the IEEE/Photonics Society. He has been served as a Technical Program Committee (TPC) Member of the electrical subsystems' category for the Optical Fiber Communication Conference from 2016 to 2018. He has been currently serving as a TPC Member for "Point-to-Point Optical Transmission" category for the European Conference on Optical Communication since 2018.

Junho Cho (Senior Member, IEEE) received the B.S., M.S., and Ph.D. degrees in electrical engineering and computer science from Seoul National University, Seoul, South Korea.

He worked at Bell Labs, Seoul, from 2010 to 2014, and Bell Labs, Holmdel, NJ, USA, from 2014 to 2020. He has been with Bell Labs, Murray Hill, NJ, USA, since 2020. He was a Ph.D. Dissertation Committee Member of Seoul National University. He has authored or coauthored numerous papers. His current research interests include probabilistic constellation shaping, forward error correction, and signal processing.

Dr. Cho serves as a technical committee member for several IEEE/Optica flagship conferences and serves as a frequent reviewer for a wide range of IEEE journals, the scope of which includes the optics, communications, circuits and systems, and computer. He was a recipient of the Excellence Research Award from Seoul National University for the Brain Korea 21 Project in 2009 and the 2021 Edison Patent Award from the New Jersey Research and Development Council, USA.

Marco Lamponi received the M.S. degree in engineering physics from the Politecnico di Milano, Milan, Italy, the M.S. degree in microelectronic engineering from the Ecole Supérieure d'Electricité, France, the M.S. degree in nanoscience and microsystems from Université Paris Sud, France, in 2008, and the Ph.D. degree from Université Paris Sud in 2012 for his work on hybrid III–V on silicon lasers for telecommunication applications.

From 2008 to 2011, he worked as a Research Engineer at Alcatel-Lucent Bell Labs (III–V lab), France, where he was in charge of both the design and the fabrication of III–V on silicon hybrid devices. From 2012 to 2013, he worked at Thales Research and Technology, Palaiseau, France, where he coordinated the fabrication of high-power semiconductor lasers and integrated photonic transceivers at subterahertz wave range. From 2014 to 2020, he worked at Huawei HiSilicon, Ghent, Belgium, where he led the silicon photonics design team developing PIC transceivers products for coherent and datacenter applications. In 2020, he was part of Nubis Communications, New York NY, USA, founding team and joined the company as a Photonics Design Leader.

Guilhem de Valicourt (Senior Member, IEEE) received the B.Sc. degree in applied physics from the National Institute of Applied Sciences (INSA), Toulouse, France, in 2008.

From 2007 to 2008, he passed the Master of Science in photonics devices at the University of Essex, Colchester, U.K. In 2008, he joined Alcatel-Thales-CEA III-V Laboratory, where he was working on the design, fabrication, and characterization of reflective semiconductor optical amplifiers and directly modulated DFB lasers toward the Ph.D. degree. In 2011, he joined Alcatel-Lucent, France, as a Research Engineer on optical communication systems. In 2014, he joined Bell Labs, Murray Hill, NJ, USA. In 2017, he became a Principal Scientist at IPG Photonics, NJ, USA, where he started the silicon photonics activities. Since 2020, he has been the Director of photonic integration with Nubis Communications, New York NY, USA, a company that he co-started. His main research interests are focused on design, characterization, and applications of advanced integrated photonics devices (in InP, silicon, and hybrid III–V on silicon platform). He has authored or coauthored more than 120 scientific papers in journals and international conferences, four book chapters, and holds more than 35 patents.

Mr. Valicourt received the 2011 Best Project Award from Alcatel-Lucent, the 2012 Marconi Young Scholar Award, the 2015 Harm Dorren Commemoration Award, and the 2019 IEEE Outstanding Young Professional Award.

Christopher R. Doerr (Fellow, IEEE) received the B.S. degree in aeronautical engineering and the B.S., M.S., and Ph.D. degrees in electrical engineering from the Massachusetts Institute of Technology, Cambridge, MA, USA.

He was a Pilot at the U.S. Air Force, Washington, DC, USA. Since joining Bell Labs, Murray Hill, NJ, USA, in 1995, his research has focused on integrated devices for optical communication. He led the silicon photonics effort at Acacia. He left Acacia at the end of 2020 and is now the President of Doerr Consulting LLC, Middletown, NJ, USA.

Dr. Doerr is a Fellow of the Optical Society (OSA) and Bell Labs. He was the Editor-in-Chief of IEEE PHOTONICS TECHNOLOGY LETTERS from 2006 to 2008. He received the IEEE William Streifer Scientific Achievement Award in 2009 and the IEEE Photonics Award in 2020. He was the Technical and General Chair of the Optical Fiber Communication Conference (OFC). He received the OSA Engineering Excellence Award in 2002.